TALLINNA TEHNIKAÜLIKOOL
TALLINN UNIVERSITY OF TECHNOLOGY

Department of Materials and Environmental Technology

Gold nanoparticles decorated ZnO nanostructured layers by hydrothermal growth for photocatalytic applications

Hüdrotermiliselt kasvatatud kuldnanoosakestega kaetud ZnO nanostruktuursed kihid fotokatalüütilisteks rakendusteks

MASTER THESIS

Student:	Kirill Balmassov
Student code:	163116KAYM
Supervisor:	Dr. Tatjana Dedova, Research Scientist
Co-Supervisor:	Dr. Atanas Katerski, Research Scientist

Tallinn, 2018

AUTHOR'S DECLARATION

Hereby I declare, that I have written this thesis independently.

No academic degree has been applied for based on this material. All works, major viewpoints and data of the other authors used in this thesis have been referenced.

"......."................... 2018.

Author: ....
/ signature /

Thesis is in accordance with terms and requirements

"......."................... 2018.

Supervisor: ....
/ signature /

Accepted for defence

"......."...................2018.

Chairman of theses defence commission ....
/ name and signature /

Department of Materials and Environmental Technology

THESIS TASK

Student: Kirill Balmassov, 163116KAYM

Study programme: KAYM09/09 – Materials for Sustainable Energetics

Main speciality: Materials for Sustainable Energetics

Supervisor: Research Scientist, Dr. Tatjana Dedova, 620 3369

Co-Supervisor: Research Scientist, Dr. Atanas Katerski, 620 3369

Thesis topic:

(in english):   Gold nanoparticles decorated ZnO nanostructured layers by hydrothermal growth for photocatalytic applications

(in estonian):   Hüdrotermiliselt kasvatatud kuldnanoosakestega kaetud ZnO nanostruktuursed kihid fotokatalüütilisteks rakendusteks

Thesis main objectives:

1. To synthesize ZnO_R by cost-effective hydrothermal growth method and cover them by gold nanoparticles using a solution with different concentration of Au

2. To study the morphological, structural, optical properties and photocatalytical properties of obtained ZnO and ZnO:Au structures

3. To figure out the optimum deposition conditions for ZnO:Au structures from those sample that gave the maximum photocatalytic efficiency.

Thesis tasks and time schedule:

No	Task description	Deadline
1.	Study of basic research methods	1st sem.
2.	Literature overview	2-3rd sem.
3.	Experimental part	4th sem.

Language: Enlglish   **Deadline for submission of thesis:**   "14" may 2018

Student: Kirill Balmassov   ....……............   "......." 2018

/signature/

Supervisor: Dr. Tatjana Dedova ....……............   "......."....................2018

/signature/

CONTENT

4

PREFACE

All work on the thesis was made in Tallinn University of Technology in Laboratory of Thin Film Chemical Technologies at the Department of Materials and Environmental Technology. The topic of the thesis was initiated by Dr. Tatjana Dedova and assisted by Dr. Atanas Katerski, to whom I express great gratitude for the advices and support.

This study aims to synthesize highly c-axis oriented vertically aligned hexagonal ZnO nanorod-like crystals via a facile and low-cost hydrothermal method for photocatalysis. In order to improve the pohotocatalytic performance of the ZnO rods (ZnO_R), gold nanoparticles (Au-NPs) were deposited over the rods surface. Au nanoparticles were obtained by spin-coating of $HAuCl_4$ in ethanol solution over the nanorod samples. Obtained Au-NPs decorated ZnO_R layers were tested on photocatalytic activity of methyl orange degradation. The photocatalytic activity of Au-NPs decorated ZnO_R exceeded the photocatalytic activity of bare rods about 10%. For example, the photocatalytic activity of ZnO_R without gold nanoparticles was 80% for 3 hours, whereas gold particles decorated ZnO_R showed higher PA activity degrading 90% of methyl orange for 3 hours. The optimum concentration for most efficient PA performance is 0.01 mol/l $HAuCl_4$. According to SEM analysis, the average size of Au-NPs on ZnO_R increases from 15 nm to 60 nm by increasing the $HAuCl_4$ concentration in solution from 0.002 to 0.03 mol/L. ZnO_R covered with Au-NPs shows the surface plasmon resonance band around 550 nm with increasing the $HAuCl_4$ solution concentration from 0.002 to 0.03 mol/L. The fac ile growth approach presented herein can be easily scaled up, affording a convenient method for the preparation of ZnO_R, which holds great potential for the application in photocatalysis for water purification.

LIST OF ABBREVIATION AND SYMBOLS

AM – Air-mass

AOP – Advanced oxidation process

Au – Gold

CB – Conduction band

Ce – Cerium

E_g – Band gap

H_2 - Hydrogen

h^+ - hole/positive charge

NaOH – Sodium hydroxide

HCl – Hydrochloric acid

HG - Hydrothermal growth

HMTA – Hexamethyltetramine

$HO^{\bullet}$ - Hydroxyl radical

$HO_2^{\bullet}$ - Hydroperoxyl radical

H_2O_2 – Hydrogen peroxide

$HAuCl_4$ - Tetrachloroauric acid

IR – Infrared radiation

LSPR – Localized surface plasmon resonance

MO – Methyl orange

NHE – normal hydrogen electrode

NH_3 – Ammonia

NH_4^+ – Ammonium

NP(s) – nanoparticle(s)

NIR – Near infrared radiation

O_2 – Oxygen

$O_2^{\bullet}$ – Superoxide radical anion

SEM – Scanning electron microscopy

SHE – Standard hydrogen electrode

SPR – Surface plasmon resonance

SnO_2 – Tin(IV) oxide

T -- Transmittance

TT – Total transmittance

TiO_2 – Titanium dioxide

UV- Ultraviolet radiation

VB – Valence band

VIS – Visible light radiation

Wz – Wurtzite

XRD – X-ray diffraction

Zn – Zinc

$ZnCl_2$ – Zinc chloride

ZnO – Zinc oxide

ZnO_R – Zinc oxide rod(s)

ZnO_R:Au – Zinc oxide covered with gold

$Zn(OH)_2$ – Zinc hydroxide

$Zn(NO_3)_2$ – Zinc nitrate

INTRODUCTION

Water pollution is one of the most serious ecological threats humankind faces today. Addressing these problems, to remediate the wastewater, development and implementation of advanced, low-cost, sustainable and highly efficient wastewater treatment technologies have become significant challenge for researches and engineers worldwide. Conventional water treatment systems are low efficiency for removing organic compounds and pollutants that are present in small concentrations. Such pollutants pass the treatment process unchanged and eventually are found in aqueous environment. [1]

Thus, the necessity in development of more efficient systems that combine inexpensive technology and possibility to remove these micropollutants has appeared. Advanced Oxidation processes (AOPs), such as photocatalysis is potentional environmental-friendly technological breakthrough for solving the problem of micropollutants. [2]

Among semiconductors, titanium dioxide (TiO_2) has been the most studied as a photocatalyst in past decades. Lately, zinc oxide (ZnO) has been proposed as an alternative to TiO_2 as it exhibits higher absorption efficiency across a large fraction of the solar spectrum, relatively cheaper, ease in preparation in form of diversity of nanostructures. [3] Commonly photocatalysts are used in a form of powder or nanoparticles, what allows to increase its active surface area subsequently enhancing their photocatalytic activity. However, expenses caused by the separation and recovery of the powdery photocatalyst after treatment limit its potential widespread application. Therefore, an effective solution to overcome that problem could be the photocatalyst with defined crystal structure attached to the substrate. For that reason, during last decades a strong attention from researchers have received nanostructured materials with large surface to volume ratio fixed on a different substrates.

Many strategies can be used to improve the photocatalytic performance such as modification of ZnO with noble metal nanoparticles. Noble metal such as gold (Au) enhances the light photons absorption and capture ability of photogenerated charges in photocatalysts (Au-NPs). [4]

The aims of this thesis are to synthesis and study the morphological, optical, structural and photocatalytical properties of ZnO rod layers (ZnO_R) and ZnO rods layers covered with gold nanoparticles (ZnO_R:Au). The rod layers were fabricated by hydrothermal growth technique (HGT) and gold nanoparticles (Au-NPs) were deposited onto the surface of ZnO_R by spin coating technique. Hydrothermal synthesis is a low cost, low temperature method that enables to produce high surface areas. [5] [6]

Ulatraviolet-visible (UV-VIS) spectroscopy, x-ray diffraction (XRD) and scanning electron microscopy (SEM) methods have been applied to study the materials properties and monitoring of MO degradation rate was recorded each 30 minutes to estimate the photocatalytic activity of ZnO_R and ZnO_R:Au layers.

1. LIERATURE OVERVIEW

1.1 Water pollution problem

Water is one of the most important natural resources, it covers about 70% of Earth's surface whereas 0.002% of water is available for human consumption. The world health organization reports that today one sixth of the world's population does not have access to safe water [7]. In 2025 due to population growth and water consumption in the growing industry, third part of the population will face with drinking water problem [8].

Water is used as a domestic and industrial supply, for a crop irrigation, transportation, recreation, fisheries, power generation, land drainage and flood protection, and waste disposal. Nevertheless, due to using of water in such purposes and especially in industry water receives waste discharges [9].

For today there are thousands of pollutants whose effects are of actual or potential concern. The number of pollutants increased annually, as new compounds and formulations are synthesised. Some of them find commercial applications and become significant pollutants of water during their manufacture and in subsequent use. Most effluents are complex mixtures of a number of different harmful agents, which include toxic substances of different nature, extreme levels of suspended solids, and dissolved and particulate putrescible organic matter [9].

In case of textile and dyeing industries, which use many kinds of dyes, both reactive and non-reactive, discharge large amounts of highly colored wastewater. Such effluent must be treated prior to discharge in order to comply with the environmental protection laws for the receiving waters. Generally, the methods, which are used for decolorization of wastewater are largely ineffective for removing color from the wastewaters and just efficient for meeting the limits of the laws [10].

1.1.1 Main water pollutants

Today millions different chemical substances exsists, a number that increases by about 300000 every year and application of them brings different types of pollutants:

Organic pollutants. Due to discharge of excessive quantities of organic matter, this type of pollutant is the most widespread and oldest for today. The major sources of organic pollution are sewage and domestic wastes; agriculture; various forms of food processing and manufacture; and numerous industries involving the processing of natural materials such as textile and paper manufacture [9]. One of the most important classs of organic pollutant is synthetic dyes, which is widely used in dyeing and textile industries [11]. These industries discharge their colored effluents

without proper treatment and this colored water cannot be used due to its hazardous nature [12]. One of the brightest representatives of this class is methyl orange dye (MO) (Figure 1.1). It is a carcinogenic water soluble azo dye which is widely used in textile industries, in manufacturing printing paper, and in research laboratories. Methyl orange is stable, shows low biodegradability and is soluble in water hence it is difficult to remove from aqueous solutions by common water purification methods [13] [14].
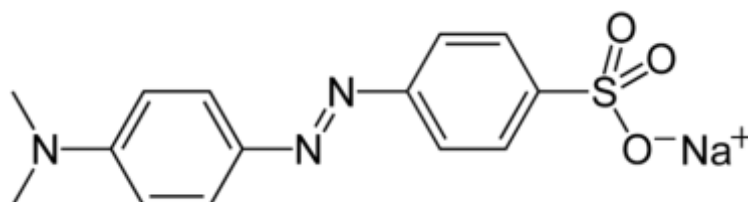

Figure 1.1 Molecular structure of Methyl Orange - $C_{14}H_{14}N_3NaO_3S$ - sodium-4-{[4-(dimethylamino)phenyl]diazinyl}benzene-1-sulfonate [14]

Heavy metals. Group of metallic elements with an atomic weight greater than 40, but excluding the alkaline earth metals, alkali metals, lanthanides and actinides. In water pollution the most important are zinc, copper, lead, cadmium, mercury, nickel and chromium. Main sources of these pollutants are industrial processes, particularly those concerned with the mining and processing of metal ores, the finishing and plating of metals and the manufacture of metal objects pigments in paint and dye, leather, rubber, textiles and paper or just prolonged contact of water with metal. Toxicity of metals depends on the amount contained in water, and in case of forming particularly hazardous organometal complexes with organic pollutants [9] [10].

Ammonia, cyanides and phenols. In combination with heavy metals these pollutants are most widespread and toxic, especially in industrialised countries. Unionised ammonia is very toxic to most organisms. Ammonia and its compounds are ubiquitous constituents of industrial effluents, because it can be used as raw material and also could be as end-product. Cyanides as well as ammonia are common materials in industry and their toxicity depends on the pH of water and as consequence of dissociation can form with metals toxic compounds. Phenolic substances include the monohydric phenols and the dihydric phenols including catechols and resorcinols. Phenolic substances rarely occur as pollutants except as components of complex effluents, which contain a variety of other pollutants [9].

Pesticides. This group of poisons of widely-varying chemicals, ranging from simple inorganic substances to complex organic molecules. Pesticides are used in agriculture as well as industry for manufacturing paper, therefore pesticides are components of many industrial effluents. Toxicity of pesticides are selective in their effects, that is they are extremely toxic to some forms of life and

relatively harmless to others. But the biggest disadvantages of pesticides that many of them are stable to chemical and biological degradation, and their persistence in the environment has for many years been a cause for concern [9].

Detergents. This group of pollutants have long molecular chains and they are not always readily broken down by sewage treatment processes. Also, some components of detergent formulations exert adverse effects of their own [9].

Antibiotics. Antibiotics are complex molecules that can have different functional groups, which display a wide range of physico-chemical and biological properties depending on the abiotic properties of the environment. These pollutants are usually found in areas with strong anthropogenic pressures such as hospital effluents. Some types of antibiotics have intrinsic high persistence, so continuous and steady introduction into the environment, aquatic or soil organisms are chronically exposed to these chemicals [15].

1.1.2 Current technologies for water treatment

The most basic conventional wastewater treatment process generally conists of separation, granular filtration (adsorption), and disinfection. Nevertheless, these main processes include wide range of techniques, which is used in water treatment process. Some of these methods cannot provide 100% purity of waste water, so basically, they should be used in a complex [12] [16].

Water treatment processes typically are classified as primary, secondary, and tertiary based on the nature of separation processes selected and outcome of the process. Generally, primary treatments are size-based separations using physical methods such as sedimentation/filtration for basic cleanup. In secondary and tertiary treatment stages, more advanced separation processes are used. The classification of advanced water treatment methods is shown in Figure 1.2 [10].
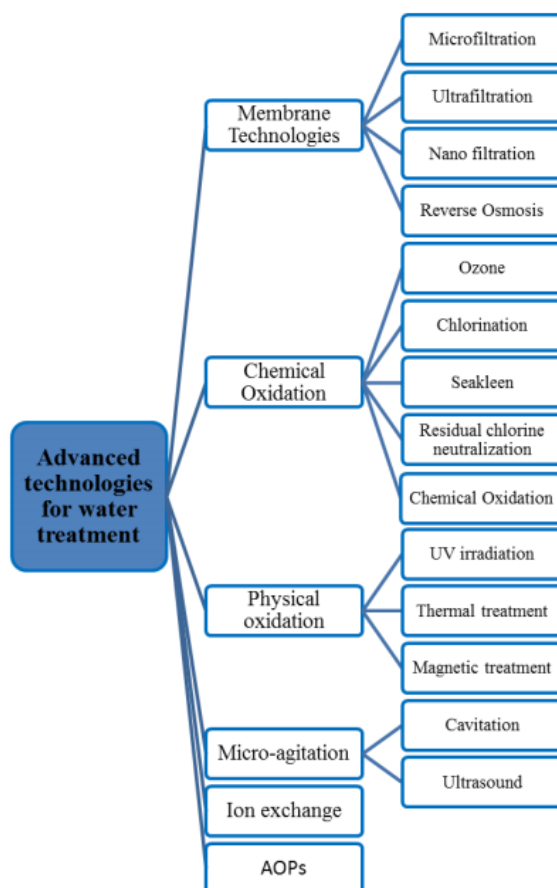
Figure 1.2 Classification of advanced water treatment technologies adapted from [16]

For most complicated pollutants, such as dye/pigment and some pesticides that are difficult to remove by using conventional methods cavitation or incineration processes are used where extreme conditions for breaking pollutant molecules are created. For heavy metal pollutants used physico-chemical methods are used such as ion exchange, membrane filtration, solvent extraction, precipitation [10].

Also, separate group of methods is united as advanced oxidation processes. This group includes techniques, such as Fenton-, ozone-, wet air- oxidations and photocatalysis. They are mainly useful for highly toxic and non-biodegradable wastes. This process operates through the generation of hydroxyl radicals and other oxidant species to degrade organic compounds in wastewater, the oxidation products are fully mineralized or less complex and can be treated by conventional biological methods. These methods are cost intensive, mainly because of high operating cost, but require much less space and many times less capital cost as compared to many of the physicochemical processes and biological processes [10].

1.2 Heterogeneous photocatalysis. Basic principles

Photocatalysis or photochemical degradation provides an eco-friendly method for removal of the pollutants from effluents [12]. This process results in a complete mineralization with an operation at milder temperature and pressure conditions. The photo-activated chemical reactions are characterized by a free radical mechanism initiated by the interaction of photons with catalyst. The photocatalytic process can be carried out by simply using slurry of the fine particles of the solid semiconductor material in a reactor irradiated with UV light [10].

Optimum operating conditions are required some calibration in terms of catalyst and pollutant amount ratio and their concentration as well as photocatalyst and pollutant nature. During the photocatalytic process also wavelength of irradiation should be taked in account, which energy should be equal or higher of the band gap energy of desided semiconductor. Moreover, the angle of incidence of the UV light should always be 90 because maximum rates are observed at this angle of incidence. Real-life industrial effluents could have different pH values, which may affect the surface charge on the photocatalyst and also the state of ionization of the substrate and hence its adsorption. Medium pH has a complex effect on the rates of photocatalytic oxidation, and the observed effect is generally dependent on the type of the pollutant and semiconductor used in the oxidation process, and, more specifically, on the electrostatic interaction between the catalyst surface and the pollutant. Also, fact which should be considered in real-life that efluents contain ionic species of different types of salts at different concentrations, which are in ionized or dissociated forms. These species can affect the adsorption process, partly absorbs UV light, which lead to decreasing of degradation rate. Also some organic compounds, for example, acetic/maleic/oxalic acids, acetone, or chloride derivatives such as chloroform are not attacked by hydroxyl radicals [10].

1.2.1 Light in photocatalytical process

The Sun is an inexhaustible energy resource freely available in all locations over the Earth surface. Therefore, the use of solar light to drive photocatalytic processes has huge potential from both environmental and economic view points [17].

Sunlight is a form of energy that consists of electromagnetic radiation in the regions of ultraviolet (UV), visible light, and infrared (IR) radiation. The solar spectrum reaching the earth's surface undergoes various absorptions in the air atmosphere, and the average solar energy falling on the earth's surface is generally known as an air-mass (which is the relative optical path length of the solar radiation, which depends from the zenith angles value) 1.5 (AM1.5) irradiation, which is equal

to approximately 100 mWcm^{-2}. In Figure 1.3 demostrated approximate shape of the solar spectrum under AM1.5 conditions and appropriate photon energy [18].
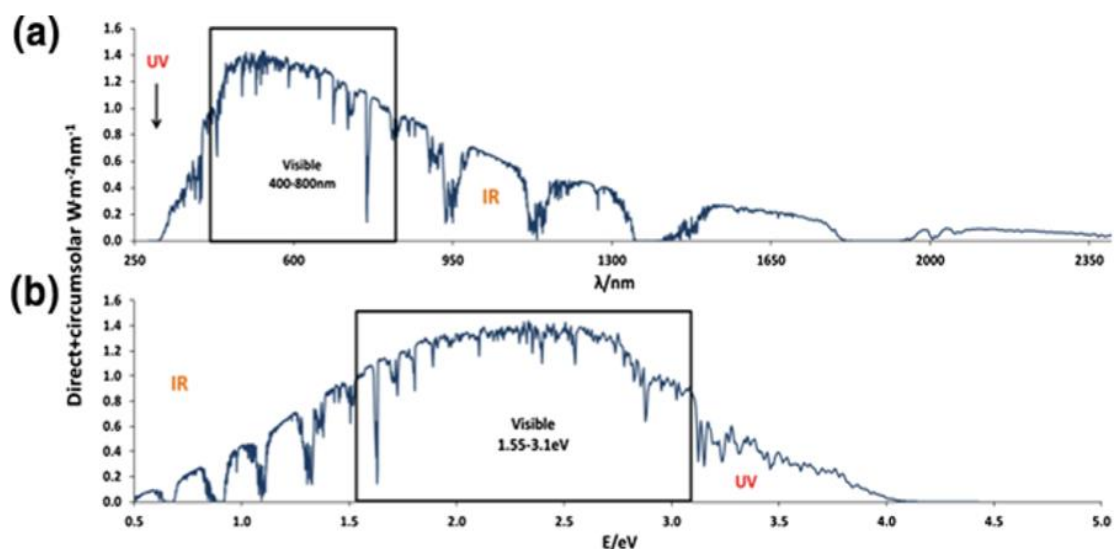

Figure 1.3 Average daily irradiance containing Ultraviolet, Visible and Infrared light plotted against wave lenght (a) and photon energy (b). [19]

The solar spectrum, displayed in Figure 1.3, contains approximately 7% UV radiation, 46% visible radiation, and 47% infrared radiation. Using this clean energy, which contains in visible and UV light, could dramatically assist a variety of reactions in a cost-effective way. Two main aspects underlay the central tenet in photocatalysis: the catalyst must be able to absorb photons preferably with a large range of energies and also react on its surface [20].

Among the wide-bandgap semiconductors suitable for photocatalytic applications, solar radiation can therefore provid the energy for promoting the excitation of electrons from the valence band to the conduction band of the semiconductor, which makes plausible the use of semiconductors for solar photocatalytic applications. Photocatalytic activity of semiconductors depends on many factors including crystalline phase, crystal size, lattice or surface defects, specific surface area, particle size, charge carrier lifetimes, or efficiency for charge transfer to molecules adsorbed on the semiconductor surface. Also, one important parameter, which is highly depent on previously listed factors is arrangement of edges of bands of semiconductor. It could be demonstrated on the sample of TiO_2 different crystalline phases, where anatase shows the highest activity in photocatalytic processes for water treatment than rutile, because of higher conduction band edge, which is responsible for photoexcited electrons with a larger reductive power [17].

1.2.1 Role of active spicies in photocatalytical process

While the electron–hole pairs are generated by the absorption of irradiation equal to or greater than the band gap, they can either recombine or migrate to the particle solution interface, where they can take part in redox reactions. In the presence of oxygen and water, a range of active spicies can be generated such as hydroxyl radical ($HO^\bullet$), superoxide radical anion ($O_2^{\bullet-}$), hydroperoxyl radical ($HO_2^\bullet$), and hydrogen peroxide (H_2O_2) at the semiconductor particle–solution interface [21]. Photocatalytic reactions proceed usually with oxygen molecules (O_2) in air, the reduction of oxygen would be the important process in photocatalytic reduction. Simply surface of the photocatalysts is covered with adsorbed water molecules in usual environments and that photocatalysts are often used to decompose pollutants in water by oxidation of water. This is important process in photocatalytic oxidation [22].

Figure 1.4 shows the schematic processes of oxygen reduction and oxidation of water near the photocatalytical particle in water. The main reactions in these processes is next: When oxygen is reduced by one electron and then it becomes a superoxide radical (Equation 1.1)

$$O_2 + e^- \rightarrow O_2^{\bullet-} \tag{1.1}$$

Superoxide form with water hydroperoxyl radical and hydroxyl ions (Equation 1.2)

$$O_2^{\bullet-} + H_2O \leftrightarrow HO_2^\bullet + OH^- \tag{1.2}$$
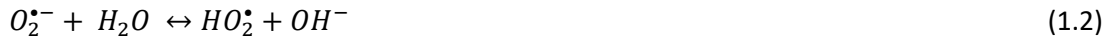
Hydroxyl ions can also form hedroxyl radicals in oxidation process with hole (Equation 1.3)

$$OH^- + h^+ \rightarrow HO^\bullet \tag{1.3}$$

In oxidation process of water, forms hydrogen ions and hydrogen peroxide (Equation 1.4)

$$2H_2O + 2h^+ \rightarrow 2H^+ + H_2O_2 \tag{1.4}$$

Further superoxide radical can be reduced by one more electrone and react with hydrogen ions or hydroperoxyl radical and form hydrogen peroxide (Equations 1.5 and 1.6)

$$O_2^{\bullet-} + e^- + 2H^+ \rightarrow H_2O_2 \tag{1.5}$$

$$O_2^{\bullet-} + HO_2^\bullet + H^+ \rightarrow H_2O_2 + O_2 \tag{1.6}$$

Hydrogen peroxide can be splitted directly by absorption of light (Equation 1.7) or by one-electron reduction (Equation 1.8) produce hydroxyl radicals [22] [23].

$$H_2O_2 + h^\vartheta \rightarrow 2HO^\bullet \tag{1.7}$$

$$H_2O_2 + e^- \rightarrow HO^\bullet + HO^-$$ (1.8)

As last step of the reaction chain active species, such as hedroxyl radicals and superoxide radical, decompose organic pollutant Equation 1.9 [24]
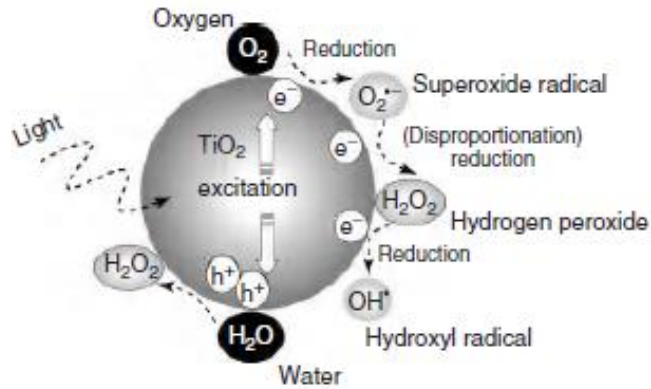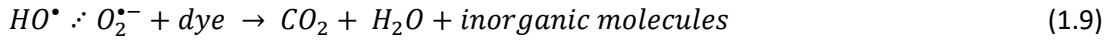
$$HO^\bullet \therefore O_2^{\bullet-} + dye \rightarrow CO_2 + H_2O + inorganic\ molecules$$ (1.9)

Figure 1.4 One electrone reduction steps of oxygen to OH radical and two-electron oxidation step of water to H_2O_2 [22]

Main reason of limitation to the rate of photocatalytic degradation is recombination of photogenerated hole–electron pairs. The rates and efficiencies of photoassisted degradation of organic pollutants are significantly improved in the presence of peroxides at low concentrations, but excess amount of peroxides can also decrease the degradation rate. The higher reaction rates after the addition of peroxide were attributed to the increase in the concentration of hydroxyl radicals and oxygen superoxide for some mid stages of degradation [23]. Basically, in photocatalytical reactions predominantly hydroxyl radicals take place, which are formed mainly from peroxides. Oxygen superoxide mainly takes part in forming of peroxides. Nevertheless, contribution of hydroxyl radicals in the photocatalytic oxidation process is not usually dominant [22].

1.3 Strategies to increase the photocatalytic performance

1.3.1 Heterostructured semiconductors

Semiconductor heterostructures are defined when two semiconductors with different electronic band structures form a heterojunction. This strategy is used to increase the lifetime of the electron-hole pairs. The most common approaches include the development of semiconductor/semiconductor hetero- structures, semiconductor/metal heterostructures,

semiconductor/carbon heterostructure. Two morphologies can be distinguished for the semiconductor/semiconductor heterostructures: the core/shell structure, and the Janus type structure, which is illustrated at Figure 1.5. In a core/shell structure, one semiconductor is completely covered by the second one. Thus, only the charge carriers injected in the external material can undergo oxidative or reductive reactions at the surface. In the Janus type structure, both materials are exposed to the environment. In this case, the two charge carriers e^- and h^+ are potentially available for oxidative or reductive reactions [25].
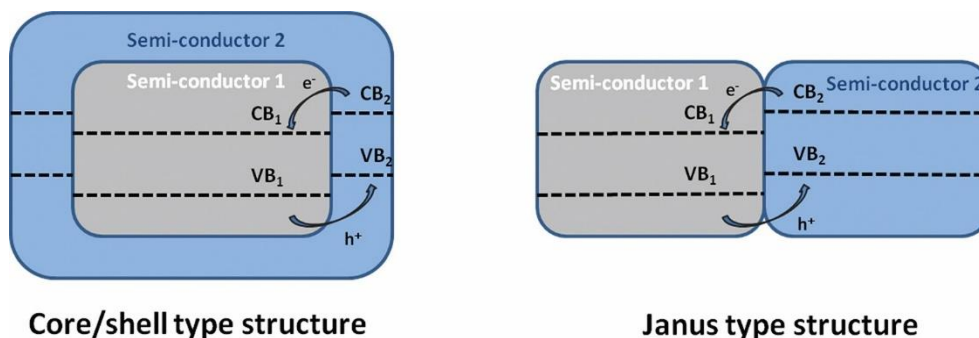
Figure 1.5 Core/shell (on the left) and a Janus type (on the right) heterostructure [25]

Nevertheless, high importance in heterostructured semiconductors have arrangement of VB and CB, which depends on the nature of semiconductor. So these energy levels is possible to arrange in energy diagramm named as physical energy scale, where the energy level of the electron in vacuum is taken as the reference point. Often electrochemical scale is used, like in case of Figure 1.6. In the electrochemical scale of electrode potentials, the potential of the hydrogen reference electrode (under standard conditions) is taken as the reference point. The difference of zero points on these scales is a constant value and is 4.44 eV [26]). Figure 1.6 illustrates arrangement of bands for some semiconductors in water solution and standard electrode potentials of some redox systems [27].
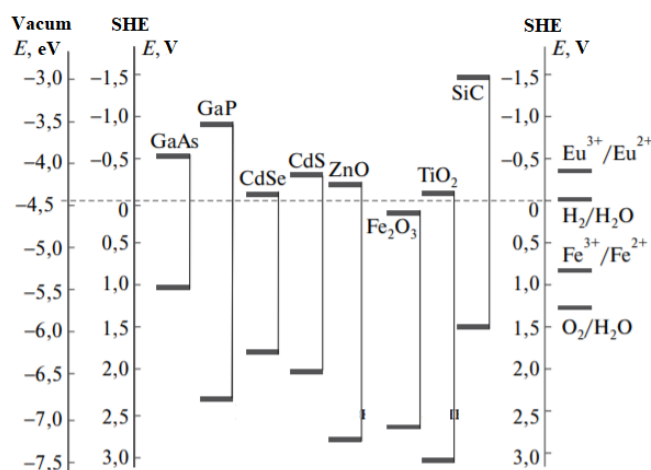

Figure 1.6 Arrangement of CB and VB for some semiconductors [27]

Potential of redox system shows the amount of energy, which is required for oxidation or reduction of speciment. So, the energy of electron will change depending on the arrangement of CB. Sample in Figure 1.7 shows the energy levels of three hypothetical semiconductors band energies. If carry out electron transfer from the valence bands to conduction bands of these semiconductors, surely the electron of semiconductor A is less energetic in comparison with that available at the valence band of semiconductor C. This is because if band position is situated at a less negative value, that is, nearer to the vacuum level, the energy of the electron would be lower as compared to those situated at more negative values. This suggests that reduction of Ce^{4+} with semiconductor C would be difficult in comparison to semiconductor A. Whereas oxidation of Ce^{3+} would occur more favorably with semiconductor C, than with semiconductor A, moreover, semiconductor B would not be suitable for either oxidation or reduction of $Ce^{4+/3+}$ [26].
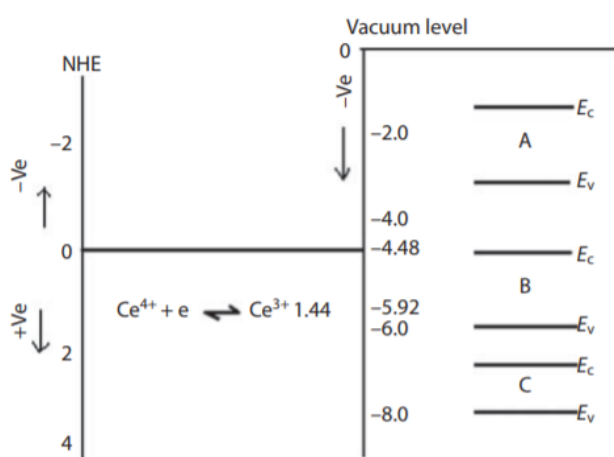

Figure 1.7 A schematic of semiconductor and redox electrolyte to show how some specific reactions can be performed only with some specific semiconductor [26]

The position of band gap in semiconductors can not be changed, but it could be modified by suitably combining two semiconductors of different band gaps [26]. It is well known that the photoexcitation of photocatalysts involves excitation, diffusion, and surface transfer of photogenerated carriers. Therefore, the carrier's lifetime is vital in determining the photoactivity during the photodegradation process. Usually, the surface properties of photocatalyst intrinsically could be influenced by the preparation method, process, and doping, which determines the surface separation and transfer of charge carriers by generating surface states where electrons and holes are spatially trapped and transferred for subsequent redox reactions [28].

The Janus type heterostructure is the most interesting one in photocatalysis as the energy gradient present at the interface allows the separation of the charge carriers on each part of the heterojunction, as represented in Figure 1.8. For a typical ZnO/SnO_2 heterostructure, the electrons photogenerated in the ZnO semiconductor with the highest conduction band energy migrate in the

conduction band of the SnO$_2$ semiconductor having the minimum conduction band energy. Whereas the holes photogenerated in SnO$_2$ semiconductor with the lowest valence band energy of migrate toward the valence band of the ZnO semiconductor having the maximum of valence band energy [25].
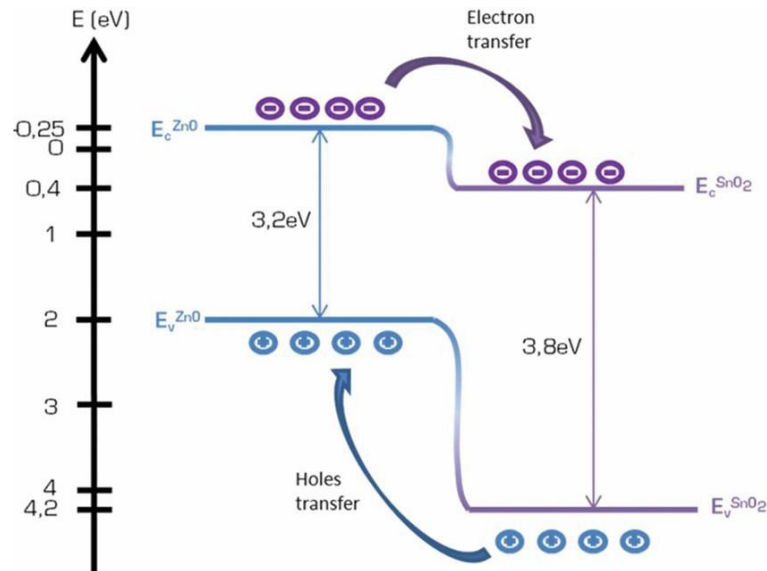

Figure 1.8 Energy diagram of ZnO/SnO$_2$ type-II heterostructure [25]

Neverthless materials, which are combined in this way should be prepeared such that the individual properties of the semiconductors are not lost. Because when such semiconductors are illuminated, electrons from the valence band of ZnO could be excited to the conduction band of SnO$_2$. Photoexcited electrons would not prefer to go to the conduction band of ZnO because this will need more energy [26].

1.3.2 Surface plasmon resonance

Surface plasmon resonance phenomenon nature stipulated by a coherent oscillation of conduction band electron driven by incident electromagnetic radiation. In metals delocalized electrons could be described as electron cloud with free electrons around positively charged nuclei. When the oscillating electric field from incident light interacts with the electron cloud, the electron cloud perturbed in way that it physically displaced from the metal framework. However Coulombic attraction from positively charged nuclei of the metal pull the electron cloud back to its initial position, so this charge polarization is shortlived. This resonant condition could be achieved when light is coupled in phase to the natural frequency of the plasmon oscillation. At these resonant conditions, the metal structures absorb the maximum amount of incident electromagnetic radiation, causing the greatest amount of charge displacement. In Figure 1.9 illustrated displacement of electron cloud under influence of electromagnetic field [29].
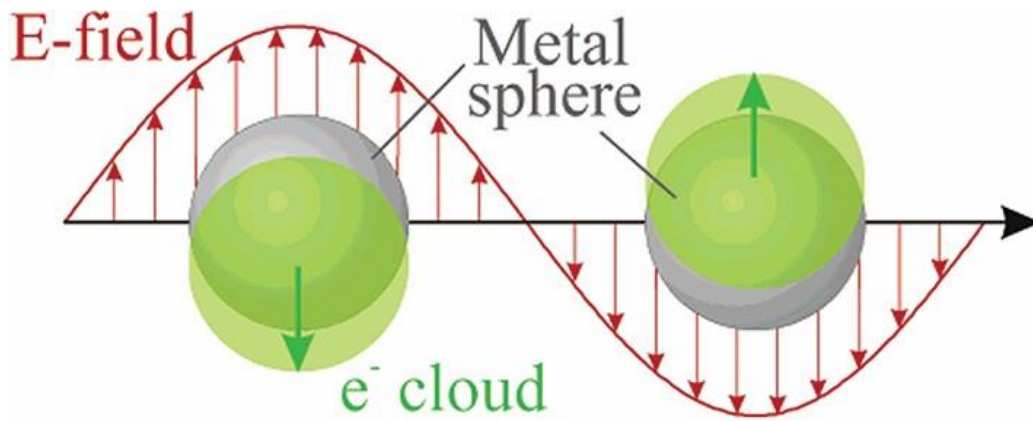
Figure 1.9 Schematic illustration of surface plasmon resonance [25]

While a variety of metals have been used to generate surface plasmon resonance (SPR), but dominated particles for SPR is gold and silver due to their stability at small sizes and strong local SPR absorption bands in the visible region of the spectrum. Many factors will affect the resonance frequency of a particle, including the material composition, size, shape, and dielectric environment [29].

In terms of promotion of photocatalytic activity LSPR depends on heterostructure used and have sence only in case, when percentage of plasmonic particles is controlled, for example, the coverage by more than 15% of metal nanoparticles inhibits the plasmonic enhancement by the reduction of the specific surface area of the semiconductor [25].

For improving the light abcorption for photovoltaics and photocatalytical applications also essential to assembly of plasmonic nanoparticles into a periodic structure. Well-controlled spacing between the plasmonic nanoparticles can induce advantageous effect on their scattering performance and their near-field due to the local coupling. Figure 1.10 illustrates the modes of light absorption on sample of photovoltaic system, where plasmonic nanoparticles periodically arranged with equal spacing [25] [30].
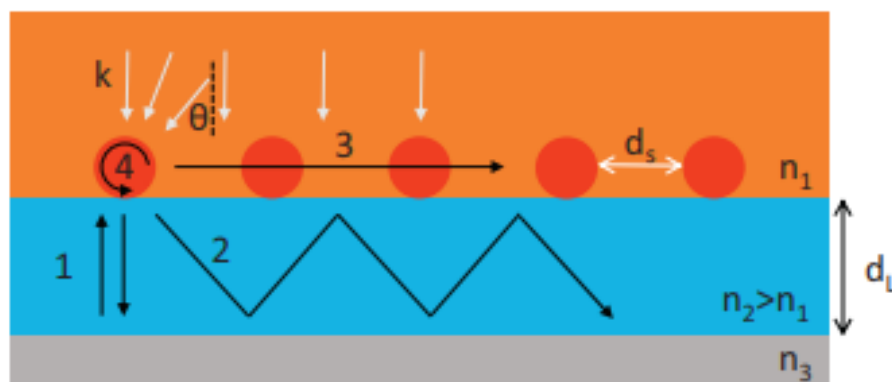

Figure 1.10 Light-tapping principles and collective optical resonances, such as: Fabry–Perot resonance (1), guided resonance (2), grating coupling (3), and Whispering gallery modes (4) [30]

This effect could be explained that, when two or more plasmonic nanoparticles are near to one another their oscillating electric fields can interact to yield new resonances. When interparticle coupling is effectively controlled, extremely high local electric fields can be generated which would otherwise not be possible with single particle [29].

1.3.3 Gold nanoparticles as promoters of photocatalytical activity

One of the effective ways to improve material chemical or physical properties is to combine two or several materials together. Noble metals, such as gold (Au) are plasmonic metals, which demonstrate good optical properties in absorption of visible light and strong localized surface plasmon resonance (LSPR) at wavelenght in the UV–VIS spectral range. Au is characterized by their strong interaction with resonant photons through excitation of LSPR derived from the collective oscillation of valence electrons [31]. It makes them suitable for serving as a photosensitizer and hence shows significant promise in heterogeneous photocatalysis. Au possible to deposit directly on a semiconductor, serving it as the co-catalyst and assist in charge carrier separation and electron trapping. The LSPR-enhanced local electric fields in the neighborhood of the nanostructure induce formation of energetic charge carriers that can be transferred to the surroundings [32].

The LSPR intensity and wavelength also depend on the size and shape of metallic nanoparticles. For example, small Au nanoparticles (<5 nm) did not exhibit any resonant behavior, whereas a sharp absorption band was observed when the size of Au-NPs was up to 50 nm [32]. An important role belongs to heterostructure architecture, for example, in Janus type heterostructure or placing particle outside of the material, Au-NPs bring double impact to local enhancement of the field comparing to placing a nanoparticle inside. In Figure 1.11 illustrated plasmonic near-field maps of TiO_2 and 50 nm sized Au-NPs sample [25].
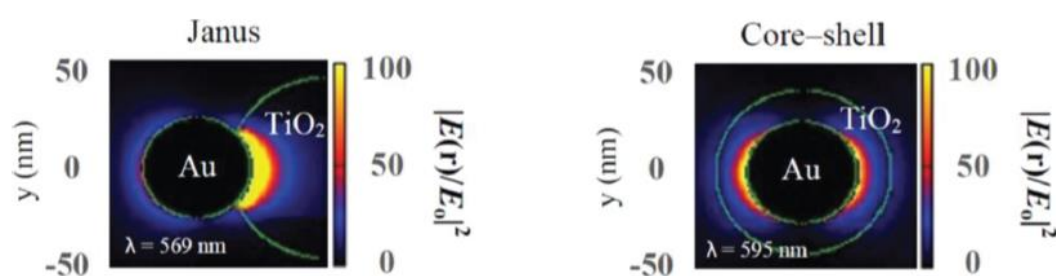

Figure 1.11 Illustration for Janus and core-shell Au 50 nm-TiO2 nanostructures and their plasmonic near-field maps [25]

In Janus structures the plasmonic near-field is localized non-symmetrically on one side of gold nanoparticle whereas in core-shell configuration (Au-core-TiO2 shell), it provides a symmetric distribution. In Janus type struture assembly the power of absorbed light was 1.75 times larger,

carrier's generation occurs closer to the TiO_2 surface, it lead to decreasing of the carrier's recombination and the carrier injection into the semiconductor is improved, than the one of core-shell and plasmonic near field is localized close to the Au-TiO_2 interface. These results confirm that plasmonic nanoparticles outside of the semiconductor material, instead of inside, result in significant improvement of the photocatalytic activity [25].

1.4 ZnO properties

ZnO is II–VI compound semiconductor and a key technological material. ZnO has a direct wide band gap of 3.4 eV in the near-UV spectral region. In its energy band structure, the bottom of the CB is formed essentially from the 4s level of Zn^{2+} and antibonding sp3 hybrid states, and the top of VB from the occupied 2p orbits of O^{2-} or from the bonding sp3 orbitals [5].

Main physical and lattice parameters are summarized in Table 1.1

Table 1.1 Properties of ZnO [6]

Propeties	Value
Lattice constants (T = 300 K)	
a_0	0.32469 nm
c_0	0.52036 nm
Density	5.67 g/cm^3
Molar mass	81.37 g/mol
Melting point	2248 K
Bang gap energy	~3.3 eV, direct
Work function	5.3 eV
Relative dielectric constant	8.66
Intristic carrier concentration	< 10^6 cm^{-3}
Exciton binding energy	60 meV
Electrone effective mass	0.24
Electrone mobility (T = 300 K)	200 cm^2/V*s
Hole effective mass	0.59
Hole mobility (T = 300 K)	5-50 cm^2/V*s

1.4.1 ZnO structure

Most of the group II–VI binary compound semiconductors crystallize in either cubic or hexagonal wurtzite (Wz) structure where each anion is surrounded by four cations at the corners of a tetrahedron, and conversely. ZnO belongs to wurtzite, with a hexagonal crystal structure, and the space group is $P6_3mc$. This tetrahedral coordination is typical of sp^3 covalent bonding nature, but these materials also have a substantial ionic character that tends to increase the bandgap beyond the one expected from the covalent bonding. The possible crystal structures shown in Figure 1.12 are wurtzite, zinc blende, and rocksalt. Under ambient conditions, the thermodynamically stable phase is that of wurtzite symmetry. The zinc blende ZnO structure can be stabilized only by growth on cubic substrates, and the rocksalt (NaCl) structure may be obtained at relatively high pressures [33].
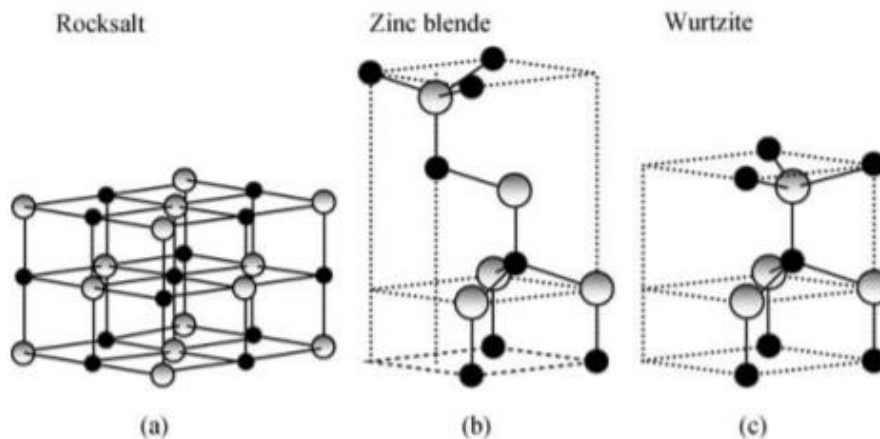

Figure 1.12 ZnO crystal structures (a) cubic rocksalt, (b) cubic zinc blende, and (c) hexagonal wurtzite (B4). Shaded gray and black spheres denote Zn and O atoms, respectively. [33]

The structure of ZnO can be simply described as a number of alternating planes composed of tetrahedrally coordinated O^{2-} and Zn^{2+} ions, stacked alternately along the c-axis (Figure 1.13). The tetrahedral coordination in ZnO results in noncentral symmetric structure and consequently piezoelectricity and pyroelectricity [5]. Another important characteristic of ZnO is polar surfaces. The oppositely charged ions produce positively charged Zn-(0001) and negatively charged O-(0001¯) surfaces gives rise to a polar repeat unit along the c-axis as well as a contradiction in a surface energy [34] [35].
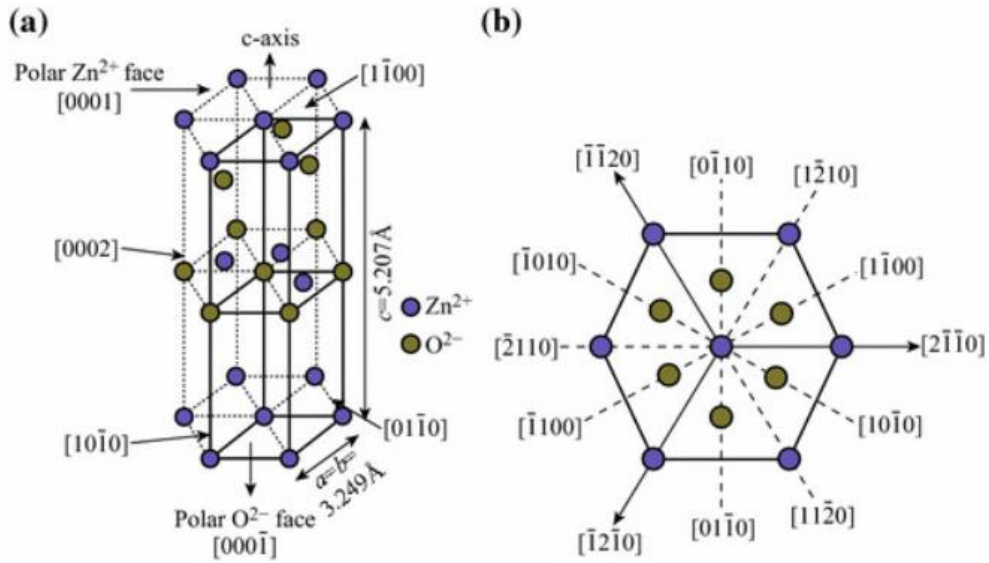
Figure 1.13 ZnO unit cell with wurtzite structure. b Various crystal planes of ZnO Wurtzite structure [35]

Structurally, ZnO has three types of fast growth directions: $[21\bar{1}0]$: ($\pm[21\bar{1}0]$, $\pm[1\bar{2}1\bar{0}]$, $\pm[1\bar{1}\bar{2}0]$); $[0110\bar{}]$: ($\pm[011\bar{0}]$, $\pm[101\bar{0}]$, $\pm[11\bar{0}0]$); and $\pm[0001]$. ZnO exhibits a wide range of novel structures that can be grown by tuning the growth rates along main fast growth directions due to atomic terminations and polar surfaces. One of the most profound factors determining the morphology involves the relative surface activities of various growth facets under given conditions. Crystal has different kinetic parameters for different crystal planes, which are emphasized under controlled growth conditions. So, after an initial period of nucleation, a crystallite will commonly develop into a three-dimensional object with well-defined, low index crystallographic faces. Figure 1.14 shows a few typical growth morphologies of 1D nanostructures for ZnO. These structures tend to maximize the areas of the $[21\bar{1}0\bar{}]$ and $[0110\bar{}]$ facets [34].
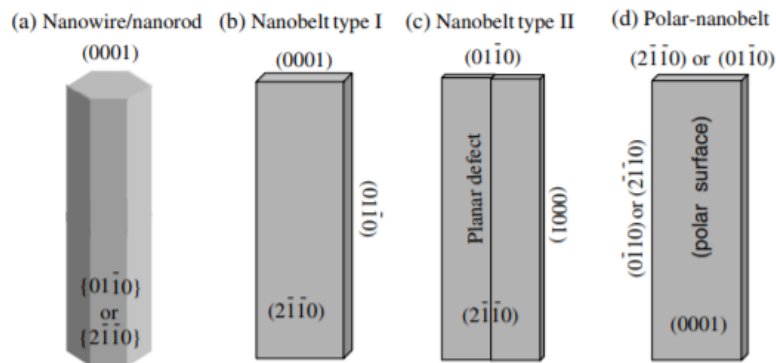

Figure 1.14 Typical morphologies of one-dimensional ZnO nanostructures and the corresponding facets [34]

26

1.4.2 Nanostructured ZnO

The dimensions of the semiconductor materials continuously shrink down to nanometer or even smaller scale and due to quantum size effects, some of physical, optical and chemical properties of semiconductors are changed [6]. Also, nanoparticles surface areas are higher, which promote absorbing of higher amounts of pollutants onto the phocatalyst surface and increasing the surface area of light absorbance by the photocatalyst [36].

Main factors, which affect the morphology of the ZnO, for example, morphology of the substrate as well as controllable synthesized parameters, such as deposition temperatures, pressures, carrier gas flux and deposition method by itself. Through these factors diverse nanostructures such as nanowires, nanorings, nanobelts nanorods and so on have been produced (Figure 1.15) [34].
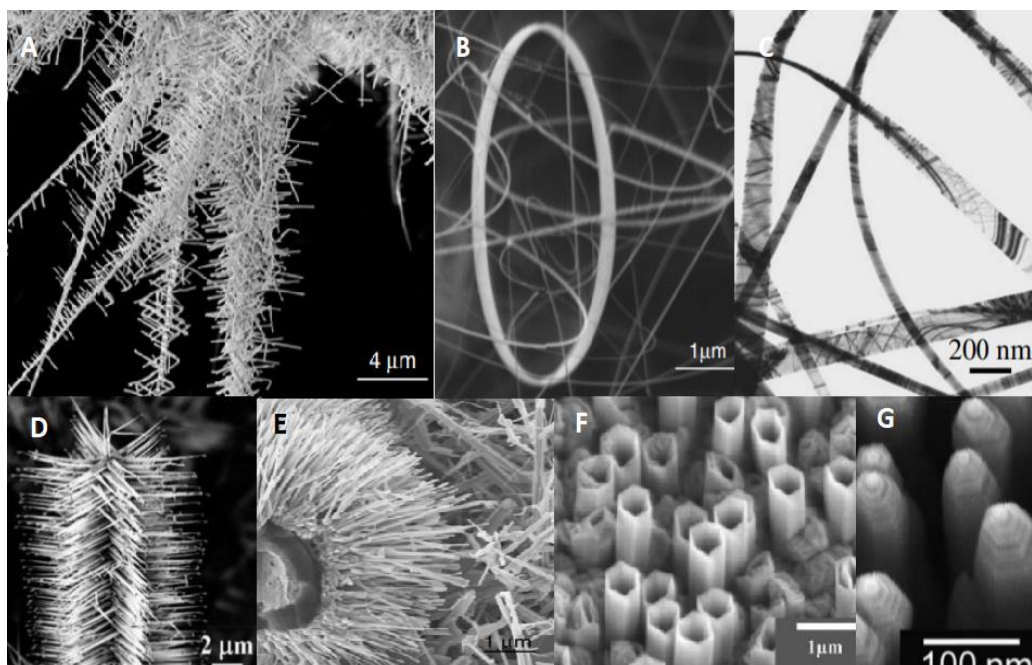

Figure 1.15 Illustration of various nanostructures A - hierarchical nanowire, B - nanoring, C – nanobelt, D - nanopropeller, E - nanonails and wires, F - nanotubes, G – nanorods, adapted from [34] and [33]

1.5 Applications of ZnO

ZnO is a very promising material for wide rage of semiconductor applications. For example, the lack of a centre of symmetry in wurtzite, combined with large electromechanical coupling, results in strong piezoelectric and pyroelectric properties and the consequent use of ZnO in mechanical actuators and piezoelectric sensors [34]. In addition, ZnO is a wide band-gap compound semiconductor that is suitable for short wavelength optoelectronics in the blue/UV region, including light-emitting diodes, laser diodes and photodetectors. Since the oscillator strength of

excitons is typically much larger than that of direct electron–hole transitions in direct gap semiconductors [37].

Nanostructured ZnO is prominent photocatalyst candidate to be used in photodegradation of organic pollutants, owing to the facts that ZnO is low-cost, non-toxic and more efficient in the absorption across of the solar spectrum compared to TiO_2 [38].

ZnO nanobelt demonstrates to be a promising material as nanoresonator and nanocantilever. Its small size renders improved sensitivity compared with conventional cantilever fabricated by microtechnology. Manipulation of ZnO nanobelt to desired length and position shows the prospect of its application as a highly sensitive atomic force microscopy (AFM) cantilever [6].

1.6 ZnO deposition methods

ZnO nanostructures and films with uniform thickness and orientation have been grown on a variety of substrates using different deposition methods, including vapour phase deposition methods, liquid-phase reaction methods, patterned growth and wet-chemical methods [5] [37].

The synthesis of ZnO nanostructures through liquid-phase reaction methods can be classified as hydrothermal, solvothermal and electrodeposition methods. Also, this method group includes techniques such as template method, sol-gel teqnique, spray pyrolysis [5].

For deposition of ZnO layers spray pyrolysis technique and hydrothermal growth technique (HGT) are used.

1.6.1 ZnO flat surface by spray pyrolysis technique

Spray pyrolysis is a very simple, non-vacuum and inexpencive processing method for preparing plain and nanostructured layers with precise composition control and stoichiometry, high crystallinity and purity of the materials [39]. Moreover, it is useful for producing large scale films. The quality and physical properties of films prepared by using spray pyrolysis technique depends on the deposition conditions such as the nature and concentration of precursor, substrate temperature, spray rate, nozzle to substrate distance, pressure of carrier gas, and annealing. In these parameters, substrate temperature usually plays a critical role in the growth of ZnO films [40].

Typical spray pyrolysis equipment shown in Figure 1.16 and consists of an atomizer, precursor solution, substrate heater, and temperature controller. Thin-film deposition, using the spray pyrolysis technique, involves spraying a metal salt solution onto a heated substrate and undergos a thermal decomposition. Spray pyrolysis involves many processes occurring either simultaneously or sequentially and can be divided into three main steps: atomization of the precursor solution,

transportation of the resultant aerosol, and decomposition of the precursor on the substrate. The most influent step in spray pyrolysis technique is decomposition of precursor, because it depends on the temperature ofsubstrate, transported solution can achieve the substrate in different phases. This facror is critical in growing of high quality thin films [41].
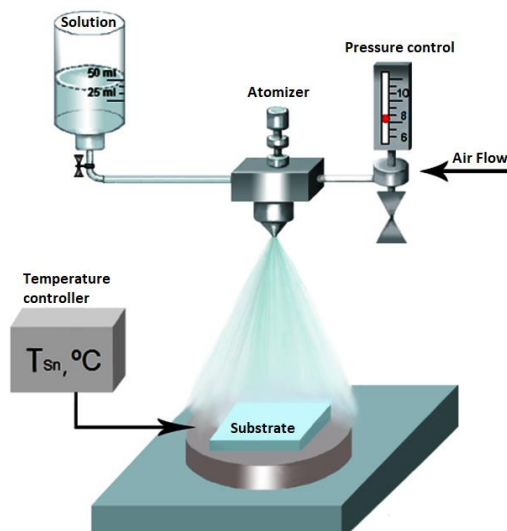

Figure 1.16 Spray pyrolysis equipment

Spray pyrolysis method was used in this study to produce ZnO flat films as seed layers prior the growth of ZnO rods by hydrothermal growth technique.

1.6.2 Hydrothermal growth of ZnO nanostructures

The term "hydrothermal" has a geological origin, where it implies a regime of high temperatures and water pressure. For hydrothermal reaction simply used autoclave reactor with thick-walled steel cylinders with an airtight seal which must be able to withstand high temperatures and pressures for prolonged periods. Inside the cylinders, inert liners are inserted usually made of Teflon or other anticorrosive material. These liners serve as the vessels inside which the reaction takes place. The principle relies on the fact that the reaction mixture inside the line/autoclave needs to be heated in order to create two temperature zones. The chemical dissolves in the hotter zone, and the saturated aqueous solution in the lower part is transported to the upper part by convective motion of the solution. The cooler and denser solution in the upper part of the autoclave descends, while the counterflow of solution ascends. The solution becomes supersaturated in the upper part as the result of the reduction in temperature and crystallization sets in. This technique has many advantages in that the products that are inevitably powders can be formed directly from solution. Moreover, the process is able to control the particle size, shape, and chemical composition, stoichiometry in a relatively facile manner [20].

Hydrothermal technique is the most common synthesis method for ZnO nanostructures out of the solution-based methods. Hydrothermal synthesis has a low cost, low growth temperature and can be used for mass production [5] [6]. Under the hydrothermal conditions, water can be used as a kind of chemical constituent, and participates in the reaction of chemical composition. It can also be solvent, mineraliser and transfer media of pressure at the same time. Under high pressure conditions, the majority of reactants can be partly dissolved in water, which is of great benefit to prompting reaction in the liquid- or gas-phase. The common types of hydrothermal synthesis include hydrothermal oxidation, hydrothermal reduction, hydrothermal synthesis, hydrothermal decomposition, hydrothermal precipitation, hydrothermal crystallisation reaction, hydrothermal chemical reaction, microwave hydrothermal method, ultrasonic hydrothermal method, etc [5].

In the case of photocatalysis, this technique has shown dramatic results, especially for incorporating dopants into the oxides and also for predominantly forming highly crystalline structures. The activity of semiconductor photocatalysts depends critically on the formation of many carriers that can migrate to the surface to participate in redox reactions. As such it is imperative to avoid recombination, which for certain types of oxides predominantly seems to occur at crystal lattice defects [20].

Hydrothermal method was applied in this study to grow elongated ZnO rod-like layers.

1.6.3 Literature overview on ZnO rod-like crystals grown by hydrothermal growth method

The general procedures of synthesising crystal materials using hydrothermal reaction include the determination of reaction precursors type and theirmolar ratio, reaction temperature and pressure, deposition time [5].

1.6.3.1 Influence of precursors concentration in HG on ZnO crystals morphology

The changes of concentration of precursors in solution influence the different parameters such as a diameter and length of the nanorods as well as the whole morphology of ZnO. In Figure 1.17 different structures obtained in hydrothermal process at constant temperature and processing time are shown. As can be seen from Figure 1.17, concentration of ammonia in solution from 0.3 to 0.75 mol/L resulted in ZnO_R with small diameters and long crystals (L=2 μm, d=50 nm); high concentration of ammonia 1.2 mol/L lead to growth of fat ZnO crystals (d=200 nm). Precursor concentration influence the density and shape of the rods. Lower concentration in solution resulted in lower density of the crystals and versa versa [42].
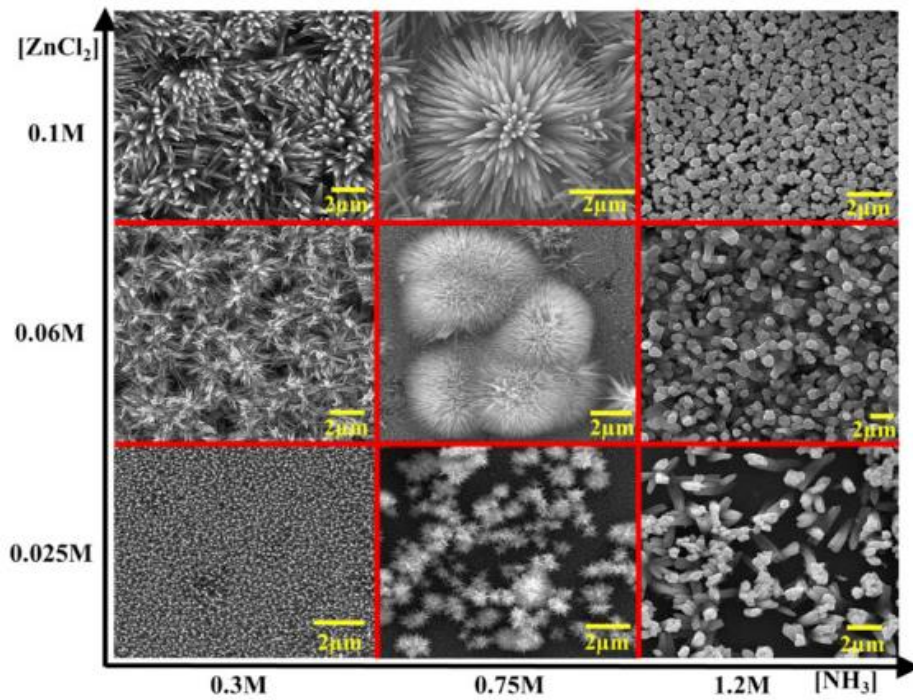
Figure 1.17 SEM images of raw materials concetrations influence to morphology of ZnO [42]

It is confirmed that concentration of precursors has very important effect on the dimension of the nanorods. As reported in [43] research, when concentration of ZnO salt ($Zn(ac)_2$) increased from 0.010 to 0.040 mol/L, the average diameter increases from 40 to 400 nm, and the average length increases from 220 to 2000 nm. In case of too high salt concentration (0.04 mol/L) obtained structure transforms into dense flat film composed of thick stacked together ZnO crystals (Figure 1.18) [43].
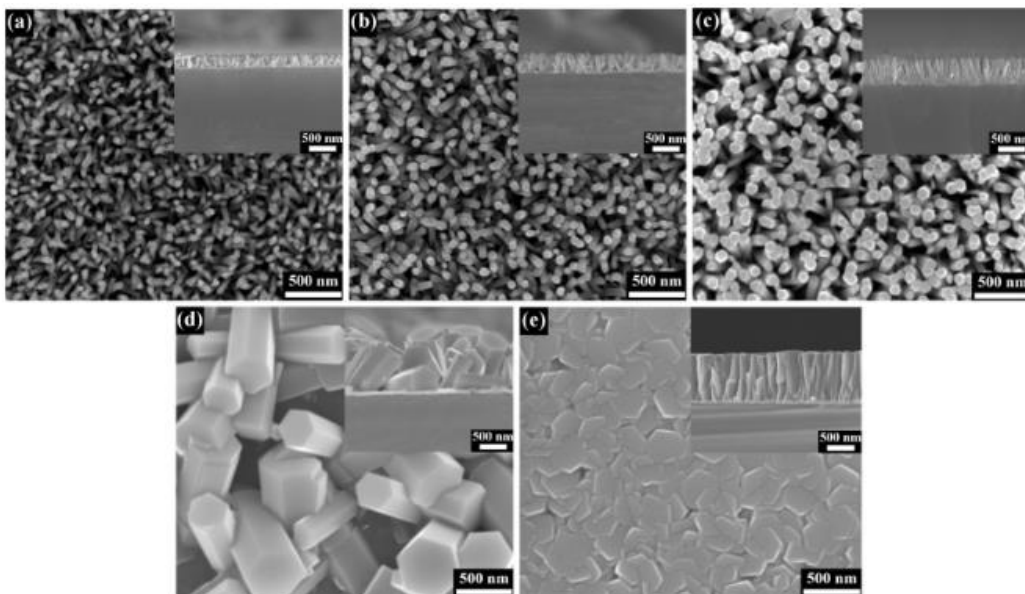

Figure 1.18 SEM images of precursor concetration influence to length and diameter of ZnO_R arrays, a - 0.010 mol/L; b - 0.015 mol/L; c - 0.020 mol/L; d - 0.030 mol/L; e - 0.040 mol/L [43]

The increase of concentration of additional precursor in solution lead to the more structural hexagonally shaped ZnO_R and their improved c-axis orientation, as reported in [44]. For example, increase of potassium hydroxide concentration in mixture with Zn salt at constant concentration of Zn salt lead to a better c-axis orientatation of ZnO_R well defined planes of hexagonal structure. (Figure 1.19)
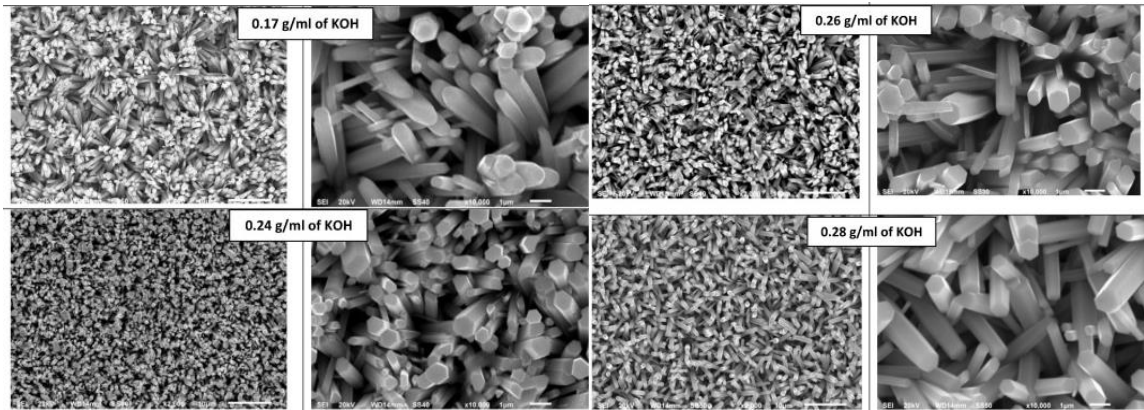

Figure 1.19 SEM images of influence of potassium hydroxide concentration onto shape of ZnO_R [44]

1.6.3.2 Influence of temperature in HG process on ZnO crystals morphology

The effects of temperature in HG process on ZnO_R morphology are reported by Ghahrizjani et al. [42] and presented as set of SEM images in Figure 1.19. According to the Figure 1.20 the average diameters of the rods increases at higher temperature, where the diameter was increased from 100 nm to 500 nm with increasing of temperatures from 75 up to 110 ^{o}C.
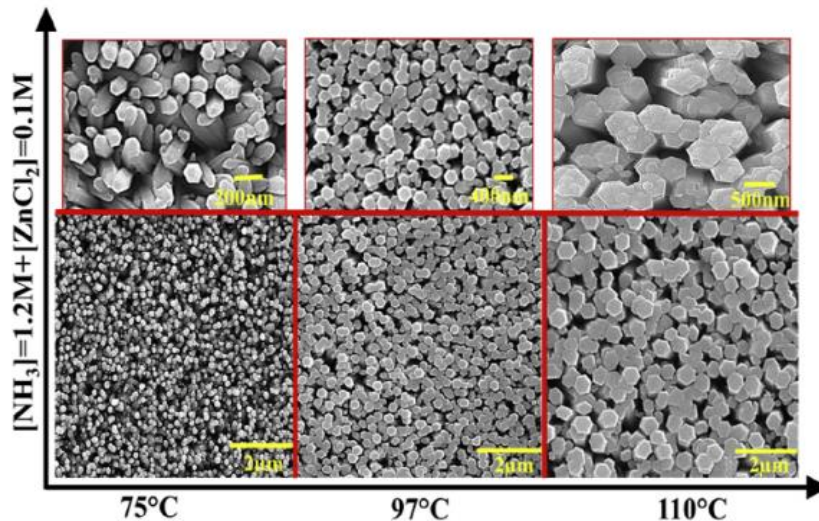

Figure 1.20 SEM images of influence of temperature on the diameter of ZnO_R [42]

Fang et al. [43] also demonstrated how drastical could be the influence of temperature on rods dimensions, from nanometer up to micrometer scale. The sets of SEM images demonstrating the effect of deposition temperature on the dimensions of the rods studied by Fang et al. [43]

Presented in Figure 1.21. As can be seen from figure, the dimensions of the rods grown at T=80 °C are L=300 nm and d=30 nm, whereas the dimensions of the rods grown at T=110 °C are L=2000 nm and d=400 nm.
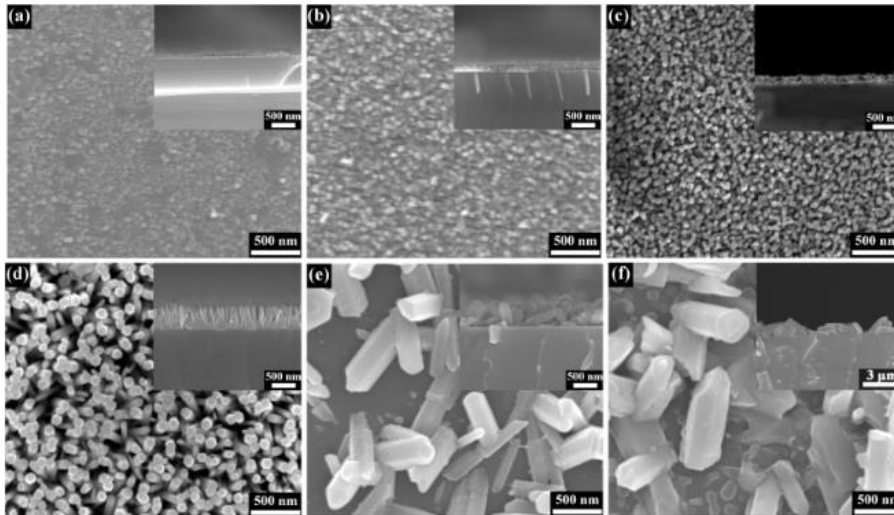
Figure 1.21 SEM images of influence of of temperature onto length and diameter of ZnO$_R$, a - T=60 °C; b - T=70 °C; c - T=80 °C; d - T=90 °C; e - T=100 °C; f - T=110 °C [43]

Another important influence of the temperature is reported in Kong, et al. [45], that the way of cooling down (fast or slow cooling) of autoclave reactor can affect the shape of ZnO$_R$ arrays. Figure 1.22 demonstrates SEM images of nanotubes and nanorods, when autoclave reactor was cooled down slowly up to room temperature ZnO nanotubes were obtained. In case of fast or immediate cooling, ZnO$_R$ arrays were obtained.
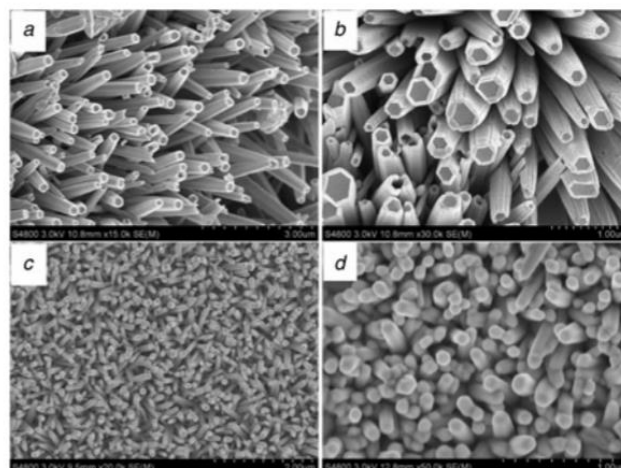

Figure 1.22 SEM images of ZnO nanostructure, where a and b – slow cooling, c and d fast cooling [45]

1.6.3.3 Influence of time in HG process on ZnO crystals morphology

Ghahrizjani et al. [42] have studied the formation of ZnO_R layers depending on the deposition time. The SEM photos of the ZnO layers grown at 60 min, 90 min and 150 minutes are presented in Figure 1.23. As can be seen from figures, the elongated separated Zno crystals were formed after one hour of deposition; further deposition of 90 minutes resulted in increased amount of ZnO nuclei giving rize to more dense coverage of the surface with ZnO crystals and longer time of 150 minutes resulted in dense compact thin film revealing rapid continuing formation of ZnO nuclei with time Thus, the time mostly affects the density of the crystals rather than their dimensions.
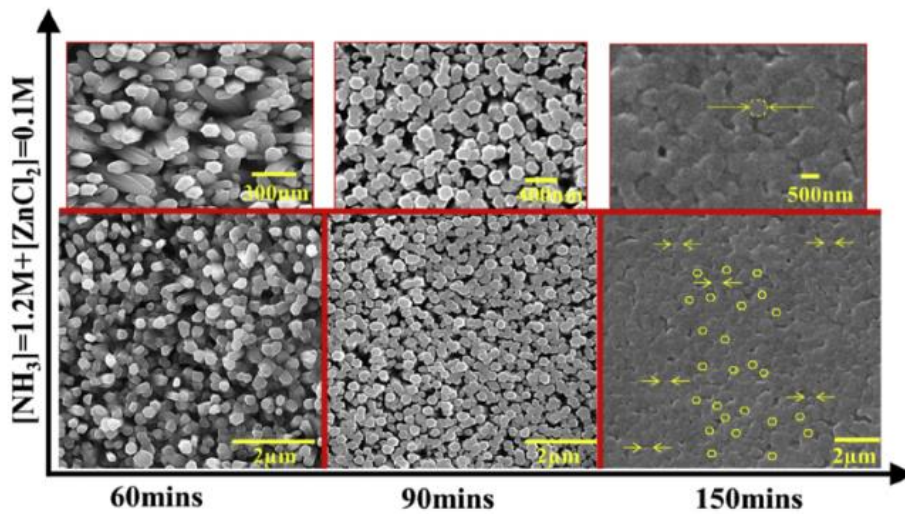

Figure 1.23 SEM images of ZnO layers deposited by HG during 60, 90 and 150 minutes [42]

1.6.3.4 Influence of other parameters in HG process on ZnO crystals morphology

Solution composition. Some additives to the main precursors in the solution can affect the rods morphology and sizes. For example, length of rod can be increased by adding polyethylenimine into the standard reaction solution of $Zn(NO_3)_2$ and HTMA. Some additives can fully change the shape of the final product, for example, if sodium citrate replaces polyethylenimine, the cylindrical round-shaped nanorods will become prismatic [5].

pH of the reaction solution. The morphology and size of the ZnO nanorods can be controlled by adjusting the pH of the aqueous solution [5] [46]. For example, obtained shapes are changed from shortened prismatic to interconnected or separated rods, as the pH of the solution changes from 7 to 11, as shown in Figure 1.24.
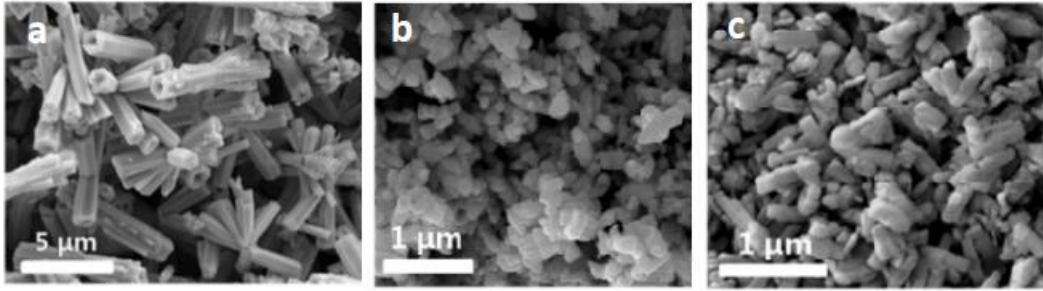
Figure 1.24 SEM images of ZnO nanostructures obtained at different pH, a – ph=7; b – ph=9; c – ph=11 [46]

Seed layer. Seed layer is usually recommended for the growth of highly structural and oriented ZnO nanostructures. According to Koo at al. study [46] in Figure 1.24 obtained structures were prepared without seed layer. In Figure 1.25 Koo, et al [46] demonstrated that seed layer lead to more structural and vertically to substrate oriented growth of ZnO_R arrays with well defined planes of hexagonal structure (if compare Figure 1.24c and 1.25 at same pH)
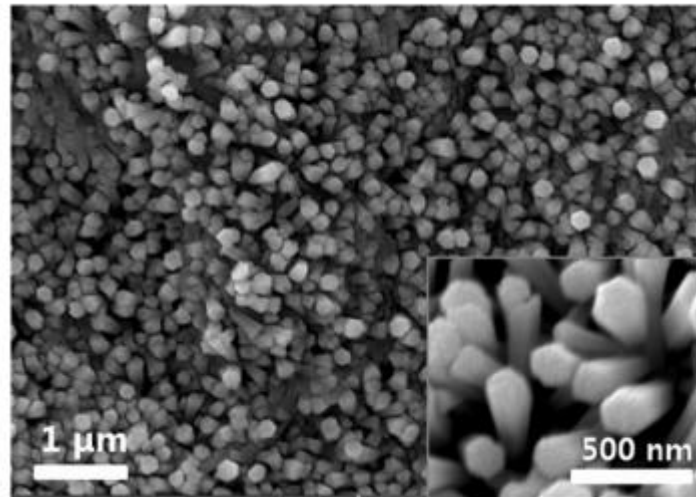

Figure 1.25 SEM image of ZnO_R prepeared with seed layer at pH=11 [46]

Also rods coverage usually repeats the seed layer uniformity or nonuniformity. For example, in case of nonuniform texture of seed layer, nonuniform coverage of ZnO layers will be obtained and versa versa. SEM figure of nonuniform substrate and its subsequent ununiform ZnO coverage is shown in figure 1.26 [47].
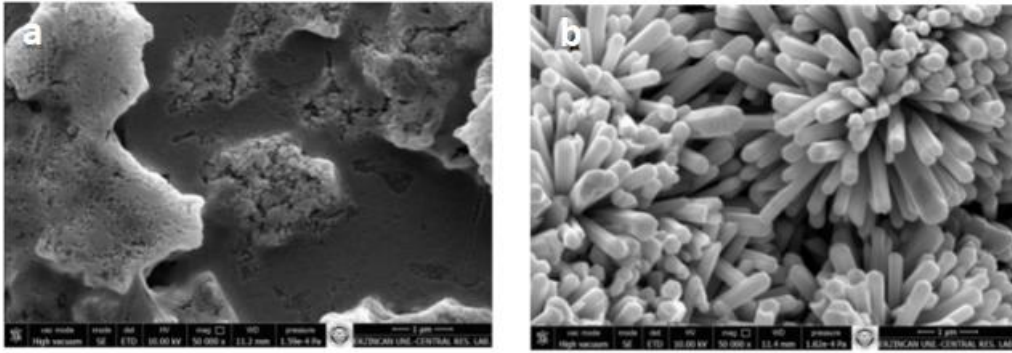
Figure 1.26 SEM images of non-uniform seed layer (a) and corresponding ZnO$_R$ arrays (b) [47]

1.6.3.5 Summary table on MO degradation rate by hydrothermally grown ZnO according to literature survey

Based on the literature survey, morphology, dimensions, mass and main deposition technological parameters of ZnO grown by hydrothermal growth versus methyl degradation rate by those ZnO layers, are summarized in Table 1.2. According to overview Table, there are many variables that influence the photocatalytic activity of ZnO, therefore it is difficult to make a precise comparison of photoctalytic activity performance.

Table 1.2 Photocatalytical activity comparison of various ZnO morphologies fabricated by hydrothermal method

Structure	Processing	Size	Amount	Raw materials	MO Conc.	Time	Degradation	Reference
Microcrystals	120˚C – 24 h	2-3 μm	100 mg	Zinc acetate dihydrate +NaOH + Cetrimonium bromide	100 mL – 1x10^{-5} mol/L	90 min	80%	[48]
Microcrystals		0.8-2.5 μm		Zinc acetate dihydrate +NaOH		50 min	99%	
Nanorods	90˚C - 1.5 h	d=500 nm l=2-2.5 μm	1 mg	Nitrate hexahydrate + HMTA	3 ml - 5 mg/L	60 min	73%	[49]
Wheatear-shaped	85˚C – 0.5 h	w=1.2 μm, l=5.8 μm	50 mg	Zinc acetate + NaOH	100 ml – 10mg/L	180 min	96,5%	[50]
Irregular polyhedron	120˚C – 8h	2-5 μm	30 mg	Triethanolamine 3,5,7 ml + zinc acetate + NH3·H2O	50 ml - 20 mg/L	180 min	62,4%	[51]
Spindle-like		5-8 μm					97,7%	
Microspheres		4-6 μm					55,8%	
Microspheres	160˚C – 12h	5-6 μm	10 mg	Zinc nitrate hexahydrate + urea	50 ml - 20 mg/L	40 min	80%	[52]
Microstars		12 μm		prev. + sucrose			100%	
Microflowers		12 μm		prev. + sucrose + trisodium citrate		30 min	100%	
Mesaporous	90˚C – 12h	15-50nm	150 mg	Zinc acetate + urea	150ml – 10 ppm	120min	80%	[53]
Micro-rods	160˚C – 8h	w=0.5-1 μm, l=3-5 μm	6 mg	Zinc powder + Tetramethylammonium hydroxide	50ml – 10mg/L	180 min	26%	[54]
firecracker-like	60˚C – 6h	w=50-80 nm, l-150-250 nm	10 mg	Zn foil+ ammonium hydroxide+ thiourea	100 ml - 1x10-5 mol/L	80 min	95%	[55]
Nanosheets	90˚C – 3h	2 μm	25 mg	Nitrate hexahydrate + hexamethylenetetramine	50 ml – 20mg/L	60 min	100%	[56]

1.7 Characterisation methods

For characterization of ZnO nanostructures SEM, XRD and UV-VIS spectroscopy were used. More detailed description of those characterization methods is given in chapters below.

1.7.1 Scanning electron microscopy (SEM)

Scanning electrone microscopy applies for study of objects that are too small to be examined by the unaided eye [57]. This microscope gives possibility to visualise objects at high resolution by means of high energy electron beam. When incident beam interracts with a solid sample for microstructural characterization, the most frequently detected signals are shown in Fugure 1.27, which are high-energy backscattered electrons, low-energy secondary electrons and X-rays, while less common signals include Auger electrons, cathodoluminescence, and measurements of beam-induced current [58].
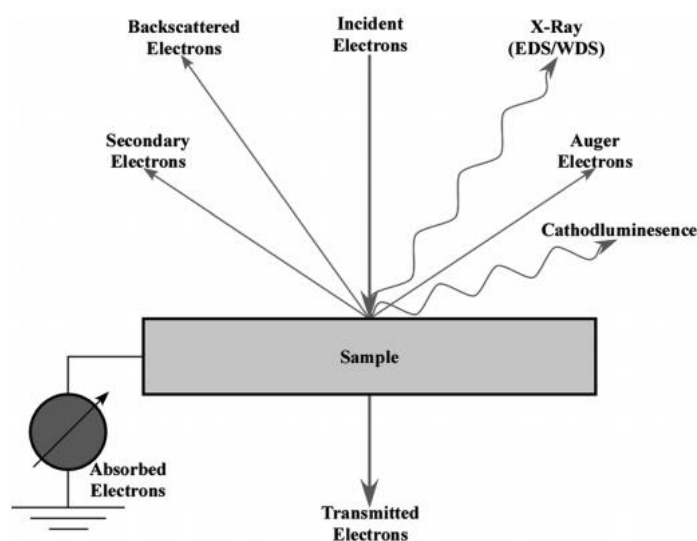

Figure 1.27 Schematic drawing of some signals created when an incident electron beam interacts with a solid sample [58]

SEM equipped with various accessories detects signals, providing an information on local chemistry, crystallography and mainly topography of specimen with high level of resolution [58].

SEM obtains the image when electron beam moves in a straight line, from point to point, forming a single line scan. After reaching the second point, the beam is deflected back along the x-axis. Then it returns to third point, displaced in the y-direction in the same row near the point one. A second line scan takes the beam to point four and the process is repeated until n lines have been scanned. This entire sequence constitutes a single frame of the raster scan. Then process repeats again from

point one and can run continuously for many frames. Obtained images can provide information about dimensions of crystals or films in the cross-section images, shape and orientation of an object [57].

For the purposes of our study SEM characterization was used in order to estimate the size, shape, density of the crystals and gold nanoparticles size and distribution over the surface of the rod crystals.

1.7.2 X-ray difraction (XRD)

About 95% of all solid materials can be described as crystalline [59]. X-ray diffraction (XRD) is one of the techniques, which reveals the information about crystal materials, also, one important feature of the x-ray microscope is that it can be used to study wet or frozen specimens, such as biological tissue or water/oil emulsions, surrounded by air or a water-vapor environment [57].

Brief work principle of x-ray microscope is next: when an x-ray beam hits an atom, x-rays scatter from them and occur x-ray diffraction. In almost all directions will occur interference, the combining waves, which are out of phase will not give resultant energy, when leaving the solid sample. Nevertheless, the atoms in a crystal are arranged in a regular pattern, and in a very few directions will occur constructive interference, waves are in phase and there will be well defined x-ray beams leaving the sample. This diffracted beams should satisfy the Bragg's illustrated with equation in Figure 1.28 [60] or when the x-rays falls under Θ angle and between different parallel planes n, scattered x-rays form more strong reflection or constructive interference at defined wavelenght λ [61].
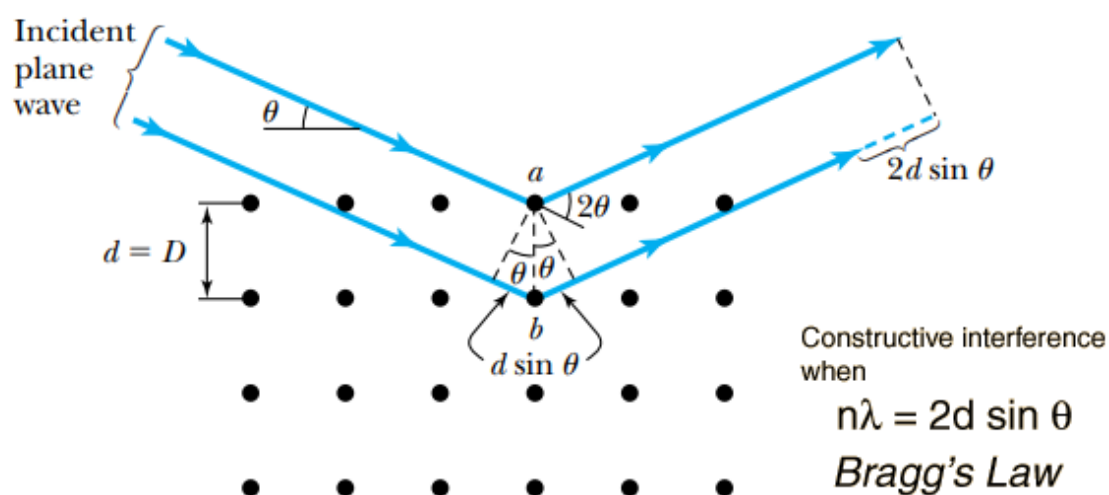

Figure 1.28 Schematic diagram illustrating x-ray scattering from Bragg lattice planes. The path difference of the two waves illustrated is 2d sin Θ. Actual scattering angle from the incident wave is 2Θ [61]

X-ray reflections from a series of parallel planes inside the crystal and their orientation with interplanar spacings are defined by the three integers h, k, l called Miller indices. One of the primary uses of x-ray diffractometry is for the determination of crystal structure. The unit cell size and geometry may be resolved from the angular positions of the diffraction peaks, whereas arrangement of atoms within the unit cell is associated with the relative intensities of these peaks [60].

1.7.3 Ultraviolet-visible spectroscopy (UV-VIS)

Spectroscopy is the study of the interaction of light with matter. The fundamental measurement obtained in spectroscopy is a spectrum, which is a plot of measured light intensity versus some property of light [62].

All the different types of light are called the electromagnetic spectrum. Each different type of light can be characterized by a different frequency, wavelength, wavenumber, or energy. The types of light listed in Figure 1.29 are the ones most commonly used in quantitative absorption spectroscopy. Every type of light is applicable for appropriate type of material [62].

$40000-14000 \text{ cm}^{-1}$ Visible & Ultraviolet	$14000 \text{ to } 4000 \text{ cm}^{-1}$ Near -Infrared	$4000 \text{ to } 400 \text{ cm}^{-1}$ Mid-Infrared	$400 \text{ to } 4 \text{ cm}^{-1}$ Far Infrared	$< 4 \text{ cm}^{-1}$ Microwaves

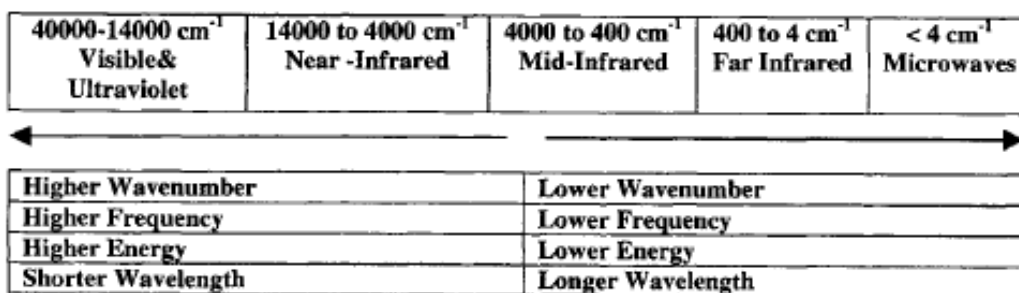| Higher Wavenumber	Lower Wavenumber
Higher Frequency	Lower Frequency
Higher Energy	Lower Energy
Shorter Wavelength	Longer Wavelength

Figure 1.29 The electromagnetic spectrum, showing the wavenumber, wavelength, frequency, and energy ranges for different types of light [62]

A spectrophotometer is an instrument for measuring the transmittance or absorbance of a sample. For concentration measuring spectrophotometer calculate the amount of light absorbed. In quantitative analysis the high concentration decreases the transmittance, because the amount of light absorbed is proportional to the number of absorbing molecules through which the light passes. Absorption of UV-VIS light is quantitatively highly accurate, because of simple linear relationship between absorbance and concentration. For accurate results, the sample to be analyzed must contain only the absorbing component for which the calibration has been performed. If the sample is a solution, a pure sample of the solvent should be used as a blank [63].

UV-VIS spectroscopy can be used to determine many physicochemical characteristics of compounds such as optical band gap by using transmittance, absorbance and reflectance characteristics, which

can provide information as to the identity of a compound through comparison of the measured spectrum with a reference spectrum [63].

Optical transmittance can be calculated by using Equation 1.10:

$$T = \frac{I}{I_0} * 100 \, ,$$
(1.10)

Where: T – transmittance, %

I – intensity of light passed through the sample

I_0 – Intensity og light falled on the sample

Through the transmittance spectrum possible to calculate absorption coeffient α using Equation 1.11:

$$\alpha d = \ln\left(\frac{I}{I_0}\right) = \ln(\frac{1}{T})$$
(1.11)

Where: α – absorbance coefficient

d – thickness of film, cm

In case of semiconductor such as ZnO absorbance coefficient possible to connect with photon energy, Equation 1.12:

$$\alpha h v = A(h v - Eg)^{1/2}$$
(1.12)

Where: A - constant

hv – photon energy, eV

Eg – band gap, eV

Eg can be calculated graphically by Tauc plot $(\alpha h v)^2$ vs. hv dependance. If part with straight line extrapolate till x-axis, where y-axis is equal to zero, this point will be equal to the Eg of the sample [61].

1.8 Summary of literature review and aims of the study

According to the literature survey, several of ZnO structures have been fabricated by HGT at different technological parameters. Most of them are in powdery non-oriented form. There are only few publications on photocatalytic application of ZnO by HTG on MO degradation (only one was found on ZnO_R:Au rods [64], where the results and parameters of samples preparation is significantly different).

There are many parameters usually changed simultaniously making comparison of the results inconvenient.

1.8.1 Aims of the study

The aims of this study are:

1. To synthesize ZnO_R by cost-effective hydrothermal growth method and to cover them by Au-NPs using a solution with different concentration of Au

2. To study the morphological, structural, optical properties and photocatalytical properties of obtained ZnO and ZnO:Au structures

3. To figure out the optimum deposition conditions for ZnO:Au structures from the samples with maximum photocatalytic efficiency.

2. EXPERIMENTAL PART

2.1 Materials and methods for samples preparation

Samples preparation contained three main steps:

1. Glass substrate preparation by cleaning and seed layer deposition
2. Hydrothermal growth of ZnO structures
3. Spin coating of Au-NPs over the surface of ZnO structures

ZnO_R layers were prepared on soda lime substrate covered with ZnO flat film seed layer. Seed layer was prepared by spray pyrolysis spraying 25 mL of aqueous solution of zinc chloride (0.1 mol/L) at Ts=470 °C. The spray pyrolysis set up is shown in Figure 2.1, for working in continuous mode was used stainless steel injector head 64-316SS from Spraying Sysetems Co. Solution was sprayed in air onto clean and heated substrate, which was placed on molten tin for good thermic contact. Compressed air was used as a carrier gas at flow rate of 8 L/min. Solution spraying rate was 0.6 ml/min and total deposition time was about 40 min.
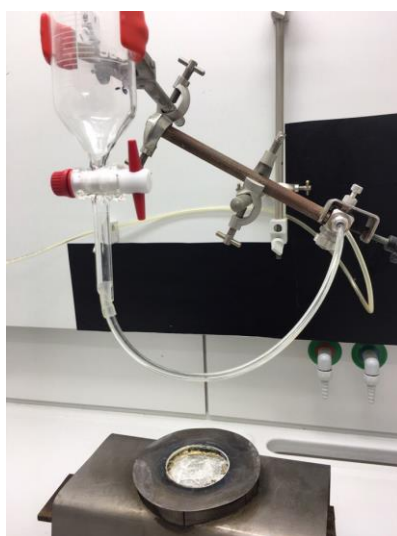

Figure 2.1 Spray Pyrolysis equipment, photo of laboratory equipment from TTU – Thin film technology laboratory

After that substrates were placed into hydrothermal (autoclave) reactor filled with equimolar aqueous solution of zinc nitrate ($Zn(NO_3)_2$) (0.1 mol/L) and hexamethylenetetramine (HMTA - $(CH_2)_6N_4$) (0.1 mol/L). The reaction took place at 120 °C for 2 hours. For hydrothermal growth of ZnO_R steel autoclave reactor Berghof BR-100 with Berghof BTC-3000 temperature controller and data logger was used (Figure 2.2).

Two of the ZnOR hydrothermally grown samples were covered by TiO_2 thin layer by spray pyrolysis by phD student Ibrahim Dündar from laboratory of Thin Films Chemical Technologies. The TiO_2

deposition parameters are published in paper [Structural and electrical characterization of TiO_2 films grown by spray pyrolysis] [65].
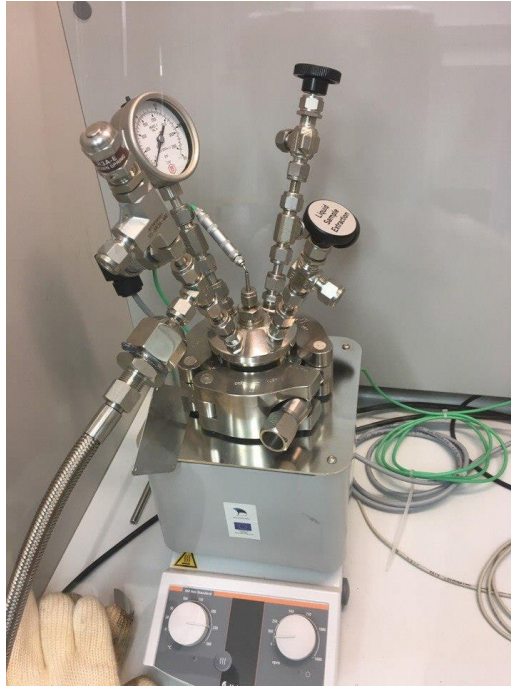

Figure 2.2 Steel autoclave reactor Berghof BR-100 from TTU – Thin film technology laboratory

The chemical reaction procedure of the synthesised ZnO nanostructures using HTMA and $Zn(NO_3)_2$ is as below:

$$(CH_2)_6N_4 + 6H_2O \rightarrow 6HCHO + 4NH_3 \tag{2.1}$$

$$NH_3 + H_2O \leftrightarrow NH_4^+ + OH^- \tag{2.2}$$

$$2OH^- + Zn^+ \rightarrow Zn(OH)_2 \rightarrow ZnO + H_2O \tag{2.3}$$

Then Au-NPs were deposited by spin coating method by dropping and spinning the tetrachloroauric acid ($HAuCl_4$ - Sigma-Aldrich 99.9%) over the rods surface. The spinning regime was 5 seconds of 500 rpm and 30 seconds of 3000 rpm. The concentrations of tetrachloroauric acid were 0.0002 mol/L, 0.01 mol/L and 0.03 mol/L. Higher concentrations were not taken according to [31], because of partial dissolution of ZnO. Then samples were dried at 100°C for 30 min and annealed at 400°C for 1 hour.

2.2 Samples characterization

1. The dimensions and shape of the rods and gold nanoparticles were studied by the high-resolution scanning electron microscope (SEM) on Zeiss HR FESEM Ultra 55 at the operating voltage 10 kV.

2. The phase composition, structure and grain sizes were studied on XRD machine. XRD patterns were recorded using a Rigaku Ultima IV diffractometer with CuKα radiation (λ = 1.5406 Å, 40 kV at 40 mA) and the silicon strip detector D/teX Ultra. The crystalline phases were identified using the XRD reference files (PDF-2 file collection) from the International Centre for Diffraction Data (ICDD, Pennsylvania, US).

3. The total transmittance (TT) spectra of the ZnO_R arrays and ZnO_R arrays with Au nanoparticles were recorded on Jasco V-670 UV-VIS-NIR spectrophotometer equipped with an integrating sphere. The spectra were taken in the wavelength range of 300-2200 nm.

4. Photocatalytic activity of the ZnO_R arrays and ZnO_R arrays with Au-NPs was estimated by the Methyl orange (MO) dye degradation rate under UV-light irradiation. MO degradation rate was monitored by changes in its concentration within the time. The concentrations of MO were measured on Jasco V-670 UV-VIS-NIR spectrophotometer. Philips Fluorescent lamp (15 W, TL-D model, λ_{max} = 365 nm) was used as UV source for photodegradation tests. ZnO rod samples-photocatalysts (substrate surface area of 9 mm^2) were mounted into 3.5 ml special UV-cuvette with 3 ml MO solution. Initial concentration of MO solution was 0.015037 mg/L. MO concentration level was recorded on UV-VIS spectrophotometer every 30 minutes. The standard measurement of MO concentration occurs at wavelength of 464 nm.

3. RESULTS AND DISCUSSION

3.1 XRD study. Structure and phase composition of ZnO layers

The crystal structure and phase composition of the samples were characterized by XRD analysis. Acquired XRD patterns of the hydrothermally grown ZnO_R crystals uncovered and covered with gold nanoparticles are shown in Figure 3.1. According to XRD patterns, all four samples composed of ZnO wurzite. Main reflections at 2Θ of 31.77, 34.42, 36.25, 47.54, 56.6° correspond to (100), (002), (101), (102) and (110) planes of hexagonal ZnO. Prevailing strong narrow reflection at 34.40° of (002) plane indicates the formation of highly crystalline, c-axis perpendicular to the substrate oriented ZnO crystals. For instance, XRD reflections intensities ratio of (002) and (101) planes of the ZnO_R grown in this study ca. 58 times higher that that for ZnO powders being I(002)/(101)=58 for ZnO_R sample compared to ZnO powder I(002)/(101)=0.4 (PDF file No. 00-036-1451).
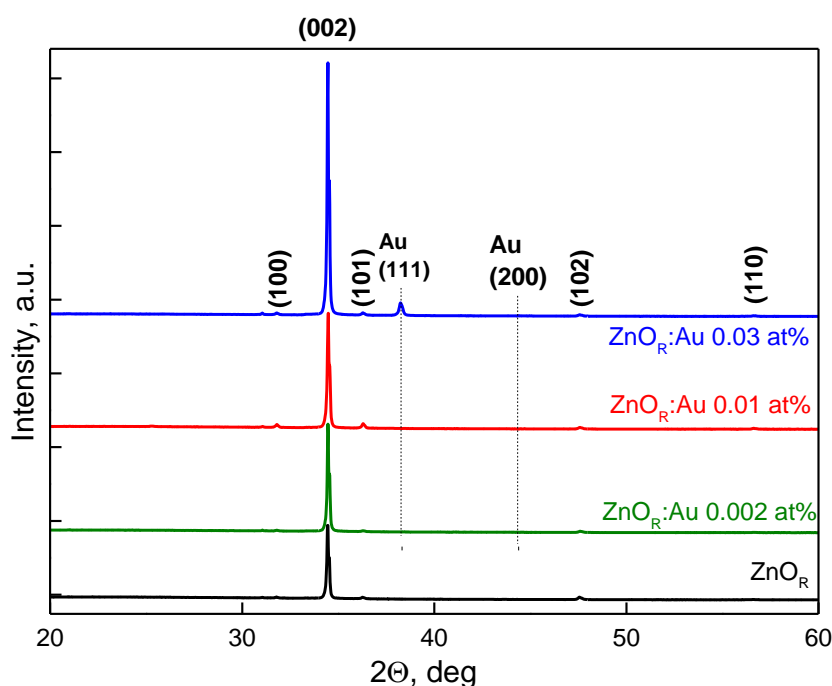

Figure 3.1 XRD patterns of HTG ZnO_R and ZnO_R covered with Au-NPs deposited from the $HAuCl_4$ solution with concentration of 0.002 mol/L, 0.01 mol/L, 0.03 mol/L

Some signs of Au nanoparticles can be detected on XRD diffractogram only for higher concentration of $HAuCl_4$ solution. Au-NPs deposited from $HAuCl_4$ with concentration of 0.03 mol/L are detectable through 2Θ at 38.1° and 44.2° corresponding to the (111) and (200) planes of metallic Au with cubic phase. Hardly ever seen XRD reflection at 2Θ at 38.1° was found for ZnO sample covered with Au

from concentration of $HAuCl_4$ solution of 0.01 mol/L. No any signs from Au-NPs were detected by XRD for the lowest concentration of $HAuCl_4$ solution of 0.002 mol/L.

3.2 SEM study. Morphology and dimensions of ZnO layers

Surface and cross-section images of the ZnO_R obtained in this study is presented in Figure 3.2. As can be seen from Figure 3.2, the rods have uniform coverage, most of the crystals have hexagon shape and well-defined vertical orientation perpendicular to the substrate, some of them have sharp (002) plane termination. The average dimension of the crystals is L=ca. 1μm, and d=50-150 nm. Au-NPs were clearly visually detected on secondary electron SEM images, where is ZnO and Au particle contrast is highly pronounced. The dimensions of Au-NPs vary with from 10 − 60 nm depending on the $HAuCl_4$ concentration. The smallest particles with d=ca. 10 nm were detected on the surface of ZnO_R coated with solution with $HAuCl_4$ concentration of 0.002 mol/L, the biggest ones d=ca. 50-60 nm with $HAuCl_4$ 0.03 mol/L. The ZnO_R crystals coverage density with Au-NPs is not very high. As can be seen from Figure 3.2, some crystals have only few Au particles on their facets.
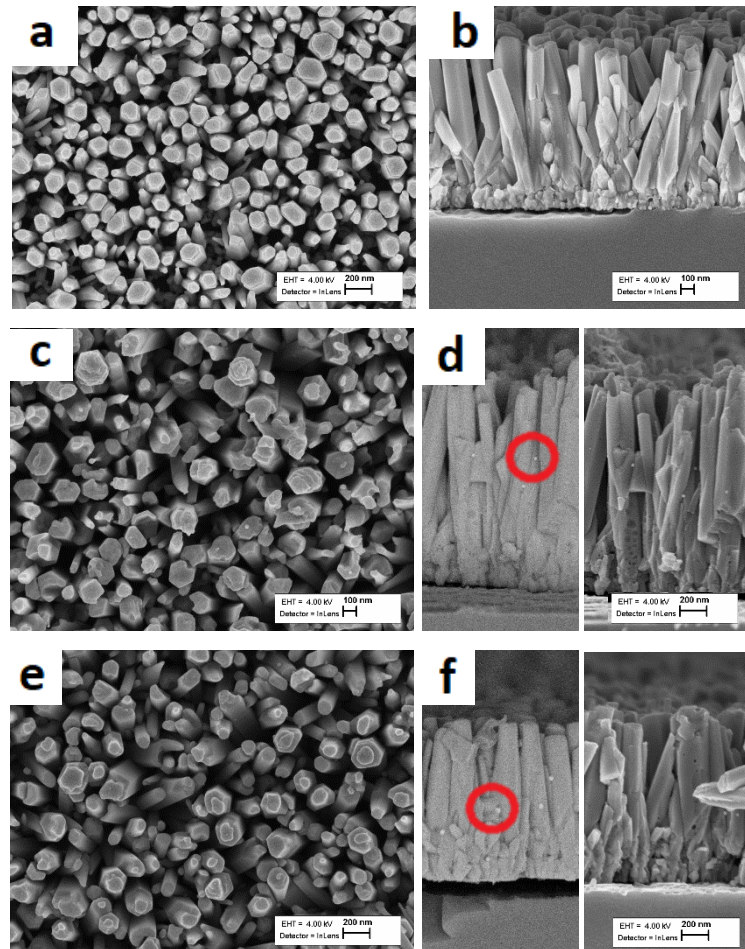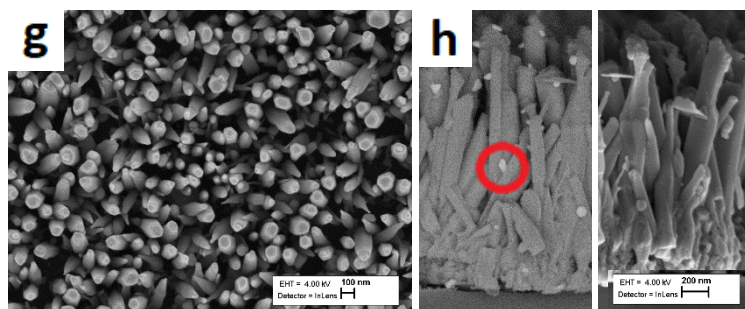
Figure 3.2 SEM and secondary electron images of ZnO rods a) ZnOR surface; b) ZnO$_R$ cross-sections; c) ZnO$_R$:Au 0.002 mol/L surface; d) ZnO$_R$:Au 0.002 mol/L cross-sections; e) ZnO$_R$:Au 0.01 mol/L surface; f) ZnO$_R$:Au 0.01 mol/L cross-sections; g) ZnO$_R$:Au 0.03 mol/L surface; h) ZnO$_R$:Au 0.03 mol/L cross-sections

In Figure 3.3 at secondary elestron images can be seen the distribution density of Au-NPs and their shape. Number of particles in case of Au precursor solution of 0.002 mol/L only 7, for 0.01 mol/L ~40 and for 0.03 mol/L 5 per 1 μm^2 square unit.

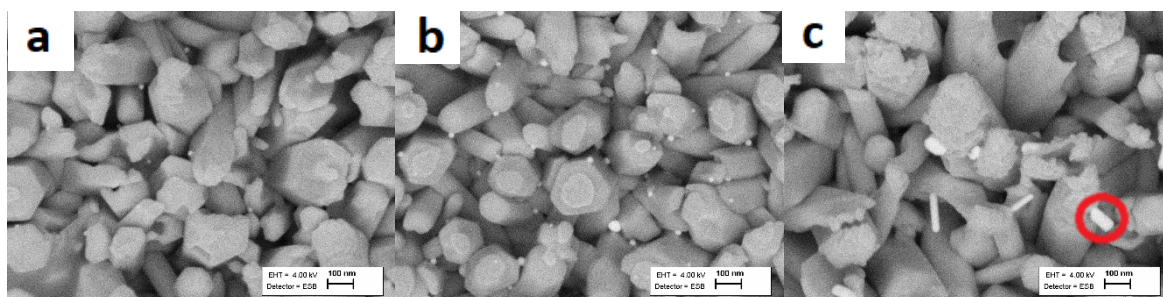Figure 3.3 Secondary electron images from the surface of of ZnO rods coveredwith Au-NPs a) ZnO$_R$:Au 0.002 mol/L surface; b) ZnO$_R$:Au 0.01 mol/L surface; c) ZnO$_R$:Au 0.03 mol/L surface

3.3 UV-VIS - optical properties

The total transmittance (TT) and total reflectance (TR) spectra of the ZnO$_R$ arrays and ZnO$_R$ arrays covered with Au-NPs were measured in the wavelength range of 300-800 nm. The TT spectra are presented in Figure 3.4. The highest total transmittance of 58% and reflectance of 33% showed the ZnO sample without gold. Au covered samples average total transmittance is around 40% and reflectance is about 17%. At wavelength of 550 nm gaps on transmittance spectra from absorption of Au-NPs can be visible on TT spectra of ZnO$_R$ 0.01 and 0.03 mol/L samples.
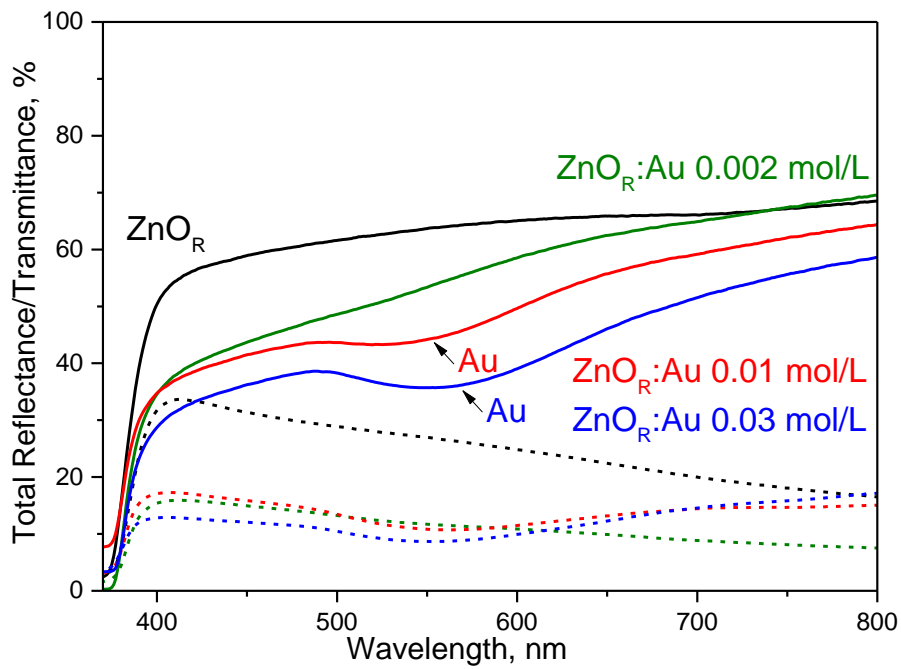
Figure 3.4 Total transmittance plots of ZnO_R arrays (left) and ZnO_R arrays with Au-NPs (right), total reflectance plats are dotted.
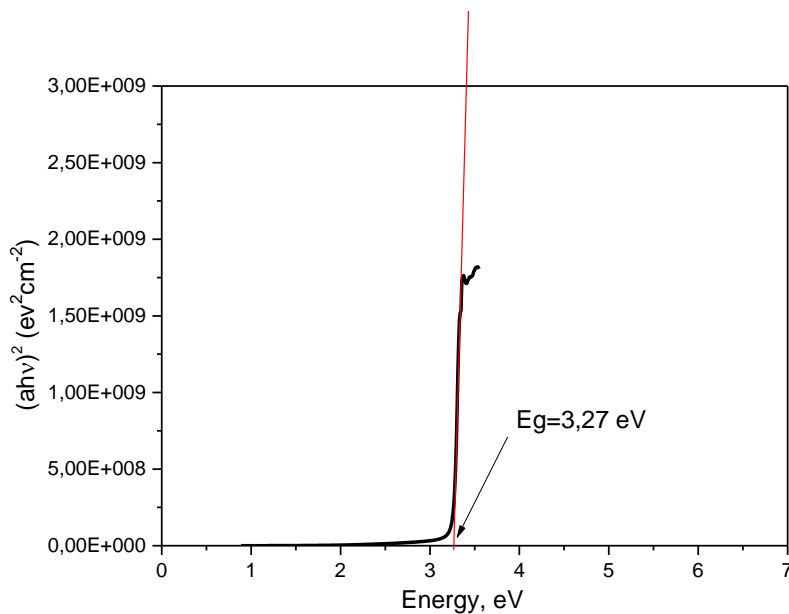

Figure 3.5 $(\alpha h\nu)^2$ vs. energy plot. Bang gap determination from Tauc´s plot.

Band gap energies were determined from Tauc´s plot as was described in experimental part. According to Figure 3.5, the right edge of the curve is nearly vertical to x-axis which indicates highly crystalline samples. The bandgap values for all the samples are presented in Table 3.1. As can be

seen from Table, independent of the gold coverage, all the samples show band gap values close to 3.2 eV, which is in good correspondence with band gap of ZnO material [66].

Table 3.1 Eg values of obtained samples

Sample	Eg, eV
ZnO$_R$	3.23
ZnO$_R$:Au 0.002 mol/L	3.23
ZnO$_R$:Au 0.01 mol/L	3.22
ZnO$_R$:Au 0.03 mol/L	3.20

3.4 Photocatalytic activity

MO degradation rate (C/C$_0$ vs. time curves) under UV light illumination without and with photocatalysts ZnO$_R$/TiO$_2$ core-shell, ZnO$_R$, ZnO$_R$:Au 0.002 mol/L, ZnO$_R$:Au 0.01 mol/L, ZnO$_R$:Au 0.03 mol/L is presented in Figure 3.6. As can be seen from Figure 3.6, the highest degradation efficiency of MO was achieved with photocatalyst ZnO$_R$ decorated with Au-NPs. Most efficient photocatalyst sample is ZnO$_R$ covered with Au from solution with concentration of HClAu$_4$ 0.01 mol/L showing the photocatalytic activity of 93.1 % for 3 hours. It seems that concentration of HAuCl$_4$ does not have strong effect on the photocatalytic performance, as photocatalytic activity values do not have big gap and logical sequence being around 90% for all three chosen HAuCl$_4$ concentrations (90.2% /3h for HAuCl$_4$ 0.002 mol/L, 93.1% /3h for HAuCl$_4$ 0.01 mol/L, 87.8% /3h for HAuCl$_4$ 0.03 mol/L). Plain, uncovered with Au-NPs, ZnO$_R$ photocatalyst has shown slightly lower MO degradation performance (79.5%/3h), compared to ZnO$_R$ covered with Au nanoparticles (ca.90%/3h). Thus, Au-NPs incorporation on the ZnO$_R$ crystals surface has increased the MO degradation afficiency approximately 10%.

Core-shell photocatalyst sample ZnO$_R$ covered with TiO$_2$ layer has shown only moderate photocatalytic MO degradation efficiency being ca. 30% for 3h what is 50% less than plain ZnO$_R$ sample.

As can be seen from the Figure 3.6, MO is not practically decomposing under UV light without photocatalyst.

To summarize, the highest MO degradation efficiency was achieved by photocatalysts ZnO$_R$ samples covered with Au-NPs.
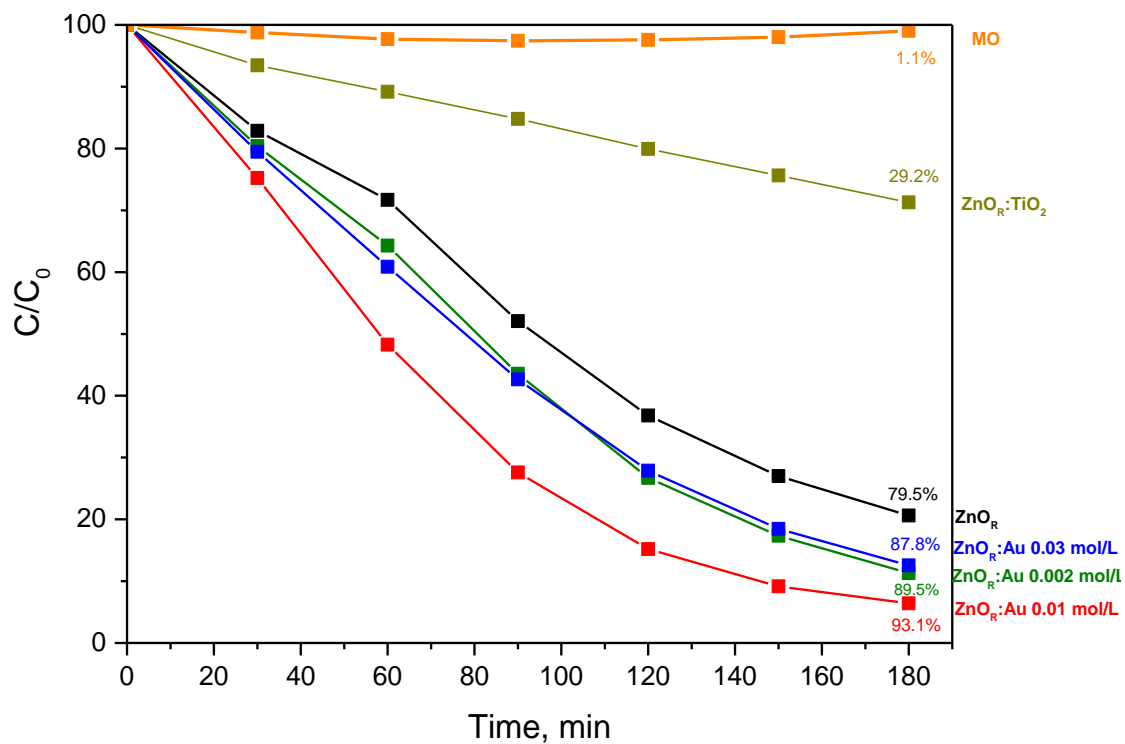
Figure 3.6 MO degradation rate (C/C$_0$ vs. time) under UV light illumination without and with photocatalysts ZnO$_R$/TiO$_2$ core-shell, ZnO$_R$, ZnO$_R$:Au 0.002 mol/L, ZnO$_R$:Au 0.01 mol/L, ZnO$_R$:Au 0.03 mol/L.

4. CONCLUSIONS

1. According to SEM and XRD studies, elongated (L=1 μm, d=50-150nm), highly crystalline and strongly (002) c-axis oriented ZnO_R and ZnO_R:Au layers were successfully fabricated by hydrothermal growth technique.

2. According to UV-VIS study, TT of ZnO_R samples is higher than TT of ZnO_R:Au layers, being 60% and ca. 50 %, respectively. Eg is around 3.2 eV for all the samples which is in a good coorespondence with theoretical Eg value of ZnO.

3. Obtained layers have shown high photocatalytic activity on MO degradation. ZnO_R:Au samples have shown increased MO photocatalytic activity compared to ZnO_R, being ca. 90%/3h and 80%/3h, respectively. Gold incorporation to the ZnO_R has increased the MO degradation efficiency approximately 10%. The record photocatalytic MO degradation efficiency of 93.1 %/3h was achieved with ZnO_R:Au 0.01 mol/L sample. Core-shell photocatalyst sample ZnO_R covered with TiO_2 layer has shown only moderate photocatalytic MO degradation efficiency being ca. 30% for 3h what is 50% less than plain ZnO_R sample.

4. Size of Au-NPs has less effect on photocatalytic activity, whereas density of Au-NPs seemed to be a significant factor that influence the photocatalytic activity of the samples.

SUMMARY

ZnO nanostructured layers composed of elongated ZnO_R (L=1 μm, d=50-150 nm) and ZnO_R covered with gold nanoparticles were sucsessfully fabricated by cost-effective hydrothermal method.

Layers were synthesized using solution mixture of HMTA and $Zn(NO_3)_2$ aqeous solutions at processing temperature of 120˚C for 2 hours. Grown ZnO_R layers vertical orientation to the substrate was achieved by means of ZnO seed layers deposited by spray onto glass substrates prior the hydrothermal deposition of ZnO_R. Au nanparticles were evently distributed over the surface of the ZnO_R layers by means of spin-coating technique. $HAuCl_4$ solution in ethanol with concentrations of 0.002 mol/L, 0.01 mol/L and 0.03 mol/L was used as a precursor for Au-NPs. After spin coating samples were dried at 100 ˚C for 30 min and annealed at 400 ˚C for 1 hour.

According to SEM studies, ZnO_R had clear hexagonal shape appearance, vertical to substrate crystals orientation, dense and uniform coverage. Size and density of Au-NPs were in a correspondence with $HAuCl_4$ solution concentration. The smallest Au-NP diemater was 10 nm and obtained from lowest studied $HAuCl_4$ solution concentration of 0.002 mol/L, the biggest ones d=ca. 50-60 nm were grown from $HAuCl_4$ with 0.03 mol/L.

According to XRD data, ZnO_R layers are highly crystalline, c-axis oriented ZnO crystals with high relative intensity ratio of I(002)/I(101)=58. (111) and (200) reflections of metallic Au (cubic) were detected on XRD diffractogram of sample covered with highest $HAuCl_4$ solution concentration of 0.03 mol/L.

The total transmittance (TT) and total reflectance (TR) spectra of the ZnO_R arrays and ZnO_R arrays covered with Au-NPs were measured in the wavelength range of 300-800 nm. The highest total transmittance of 58% and reflectance of 33% was demonstrated by the ZnO_R sample without Au. Average total transmittance of Au covered samples is around 40% and reflectance is about 17%. At wavelength of 550 nm gaps on transmittance spectra from absorption of Au-NPs can be visible on TT spectra of ZnO_R 0.01 and 0.03 mol/L samples. Band gap value of the samples not depend on the Au coverage, all the samples show band gap values close to 3.2 eV, which is in good correspondence with band gap of ZnO material.

In degradation of MO most efficient photocatalyst sample is ZnO_R covered with Au from solution with concentration of $HAuCl_4$ 0.01 mol/L showing the photocatalytic activity of 93.1 % for 3 hours. It seems that concentration of $HAuCl_4$ does not have strong effect on the photocatalytic performance, as photocatalytic activity values do not have a big gap and any logical sequence being around 90% for all three chosen $HAuCl_4$ concentrations (90.2%/3h for $HAuCl_4$ 0.002 mol/L, 93.1%/3h for $HAuCl_4$ 0.01 mol/L, 87.8%/3h for $HAuCl_4$ 0.03 mol/L). Probably, the density of Au-NPs across the sample has a more detrimental effect on photocatalytic activity. For example, the density of Au-NPs on the

photocatalytically more active sample (ZnO$_R$:Au 0.01 mol/L) was 8 times higher per 1 μm^2 square unit compared to other samples.

ACKNOWLEDGEMENTS

REFERENCES

[1] J. Fallert, H. Zhou, J. Sartor, C. Thiele, F. Maier-Flaig, D. Schneider and H. Kalt, "65 years of ZnO research – old and very recent results," *PSS,* vol. 247, no. 6, pp. 1424-1447, 2010.

[2] S. Xu and Z. L. Wang, "One-dimensional ZnO nanostructures: Solution growth and functional properties," *Nano Research,* vol. 4, no. 11, pp. 1013-1098, 2011.

[3] J. Sun, S. Tian, X. Cai, D. Xiong, S. K. Verma, Q. Zhang, W. Chen, M. Zhu and X. Zhao, "Low-temperature solution synthesis of a ZnO nanorod array with a mesoporous surface mediated by cadmium ions," *CrystEngComm,* vol. 18, pp. 8277-8283, 2016.

[4] J. Lu, H. Wang, D. Peng, T. Chen, S. Dong and Y. Chang, "Synthesis and properties of Au/ZnO nanorods as a plasmonic photocatalyst," *Physica E: Low-dimensional Systems and Nanostructures,* vol. 78, pp. 41-48, 2016.

[5] Y. Zhang, ZnO Nanostructures Fabrication and Applications, Beijing: Royal Society of Chemistry, 2017, p. 3.

[6] Z. Fan and J. G. Lu, "Zinc Oxide Nanostructures: Synthesis and Properties," *Nanoscience and Nanotechnology,* vol. 5, pp. 1-13, 2005.

[7] S. A. Alrumman, A. F. El-kott and S. M. A. S. Keshk, "Water Pollution: Source & Treatment," vol. 6, no. 3, pp. 88-98, 2016.

[8] Congressional Quarterly Inc., "Looming Wetar Crisis," *CQ Global Researcher,* vol. 2, no. 2, 2008.

[9] P. D. Abel, Water Pollution Biology, 2 ed., Sunderland: Taylor & Francis, 2014, pp. 1-3; 29-65.

[10] V. V. Ranade and V. M. Bhandari, Industrial Wastewater Treatment, Recycling, and Reuse, Elsevier, 2014, pp. 23-47; 93; 161-166.

[11] L. R. Pereira and M. S. Alves, "Dyes—Environmental Impact and Remediation," in *Environmental Protection Strategies for Sustainable Development*, 2012, pp. 112-154.

[12] S. C. Ameta and R. Ameta, Green Chemistry Fundamentals and Applications, New Jersey: Apple Academic Press, 2013, p. 205.

[13] F. P. Sejie and M. S. Nadiye-Tabbiruka, "Removal of Methyl Orange (MO) from Water by adsorption onto Modified Local Clay (Kaolinite)," *Physical Chemistry,* vol. 6, no. 2, pp. 39-48, 2016.

[14] S. Kim, P. A. Thiessen, E. E. Bolton, J. Chen, G. Fu, A. Gindulyte, L. Han, J. He, S. He, B. A. Shoemaker, J. Wang, B. Yu, J. Zhang and S. H. Bryant, Bethesda: PubChem Substance and Compound database, 2016.

[15] P. Grenni, V. Ancona and A. B. Caracciolo, "Ecological effects of antibiotics on natural ecosystems: A review," *Microchemical Journal,* vol. 136, pp. 25-39, 2018.

[16] G. Tchobanoglous, F. L. Burton and D. H. Stensel, Advanced wastewater treatments in Wastewater Engineering, Treatment and Reuse, New York: Mc Graw Hill International editions, 2003, pp. 1035-1205.

[17] J. Marugán, M. J. López-Muñoza, P. Fernández-Ibáñez and S. Malato, "Solar Photocatalysis: Fundamentals, Reactors and Applications," in *Photocatalysis: Applications*, Cambridge, Royal Society of Chemistry, 2016, pp. 92-112.

[18] I. M. Dharmadasa, Advances in Thin-Film Solar Cells, Miami: Pan Stanford, 2012, pp. 1-13.

[19] T. K. Townsend, Inorganic Metal Oxide Nanocrystal Photocatalysts for Solar Fuel Generation from Water, Davis: Springer, 2014, pp. 3-6.

[20] B. Mishra and D. Khushalani, "Nanomaterial-Based Photocatalysts," in *Nanocatalysis, Synthesis and Applications*, New Jersey, John Wiley & Sons, 2013, pp. 469-493.

[21] P. Fernández-Ibáñez, A. J. Byrne, I. M. Polo-López, P. S. M. Dunlop, P. Karaolia and D. Fatta-Kassinos, "Solar Photocatalytic Disinfection of Water," in *Photocatalysis: Applications*, Cambridge, Royal Society of Chemistry, 2016, pp. 75-77.

[22] Y. Nosaka and A. Y. Nosaka, "Identification and Roles of the Active Species Generated on Various Photocatalysts," in *Photocatalysis and Water Purification*, Weinheim, Wiley-VCH, 2013, pp. 3-20.

[23] N. Daneshvar, D. Salarib and A. Khataee, "Photocatalytic degradation of azo dye acid red 14 in water on ZnO as an alternative catalyst to TiO2," *Journal of Photochemistry and Photobiology A: Chemistry,* pp. 317-322, 2004.

[24] X. Chen, Z. Wu, D. Liu and Z. Gao, "Preparation of ZnO Photocatalyst for the Efficient and Rapid Photocatalytic Degradation of Azo Dyes," *Nanoscale Research Letters,* p. 8, 2017.

[25] O. M. Ishchenko, V. Roge, G. Lamblin and L. Damien, "TiO2 - and ZnO-Based Materials for Photocatalysis: Material Properties, Device Architecture and Emerging Concepts," in *Semiconductor Photocatalysis Materials, Mechanisms and Applications*, Luxemburg, ExLi4EvA, 2016, pp. 3-23.

[26] M. Sharon, An Introduction to the Physics and Electrochemistry of Semiconductors, Bombay: Scrivener Publishing, 2016, pp. 46; 211-212.

[27] E. A. Strelcov, Электрохимия Полупроводников, Minsk: БГУ, 2012, pp. 36-41.

[28] H. Fei, Y. Aihua and Z. Hui, "Influences of Doping on Photocatalytic Properties of TiO2 Photocatalyst," in *Semiconductor Photocatalysis. Materials, Mechanisms and Applications*, Xuzhou, ExLi4EvA, 2016, pp. 42-43.

[29] M. R. Jones, K. D. Osberg, R. J. Macfarlane, M. R. Langille and C. A. Mirkin, "Templated Techniques for the Synthesis and Assembly of Plasmonic Nanostructures," *Chemical Reviews,* pp. 3739-3741, 2011.

[30] M. Karg, T. A. König, M. Retsch, C. Stelling, P. M. Reichstein, T. Honold, M. Thelekkat and A. Fery, "Colloidal self-assembly concepts for light management in photovoltaics," *Materials Today,* no. 18, pp. 185-205, 2015.

[31] I. Gromyko, I. Oja Acik, K. Malle, T. Dedova, A. Katerski, A. Mere, V. Mikli and R. Vessart, "Surface plasmon resonance in ZnO nanorod arrays caused by gold nanoparticles for solar cell application," *Physica Status Solidi C,* pp. 1338-1343, 2015.

[32] Z. Wang, C. Chen, W. Ma and J. Zhao, "Sensitization of Titania Semiconductor: A Promising Strategy to Utilize Visible Light," in *Photocatalysis and Water Purification From Fundamentals to Recent Applications*, Willey-VCH, 2013, pp. 222-223.

[33] H. Morkoç and Ü. Özgür, Zinc Oxide Fundamentals, Materials and Device Technology, Weinheim: WILEY-VCH Verlag GmbH & Co. KGaA, 2009, pp. 1-2.

[34] Z. L. Wang, "Zinc oxide nanostructures: growth, properties and applications," *Journal of Physics: Condensed Matter,* no. 16, pp. 830-846, 2004.

[35] R. Kumar, O. Aldossary, G. Kumar and A. Umar, "Zinc Oxide Nanostructures for NO2 Gas–Sensor Applications: A Review," *Nano-Micro Lett.,* vol. 2, no. 7, pp. 97-120, 2014.

[36] Y. Yu, J. C. Yu, C.-Y. Chan, Y.-K. Che, J.-C. Zhao, L. Ding, W.-K. Ge and P.-K. Wong, "Enhancement of adsorption and photocatalytic activity of TiO2 by using carbon nanotubes for the treatment of azo dye," *Applied Catalysis B: Environmental,* vol. 61, no. 1-2, pp. 1-10, 2005.

[37] A. Janotti and C. G. Van de Walle, Fundamentals of zinc oxide as a semiconductor, Santa Barbara: IOP Publishing, 2009.

[38] C. B. Ong, L. Y. Ng and A. W. Mohammada, "A review of ZnO nanoparticles as solar photocatalysts: Synthesis, Mechanisms and Applications," *Renewable and Sustainable Energy Reviews,* p. 1, 2018.

[39] D. Klauson, I. Gromyko, T. Dedova, N. Pronina, M. Krichevskaya, O. Budarnaja, I. O. Acik, O. Volobujeva, I. Sildos and K. Utt, "Study on photocatalytic activity of ZnO nanoneedles, nanorods,

pyramids and hierarchical structures obtained by spray pyrolysis method," *Materials Science in Semiconductor Processing,* vol. 31, pp. 315-324, 2015.

[40] A. Bedia, F. Z. Bedia, M. Allerie, N. Maloufi and B. Benyoucef, "Morphological and Optical Properties of ZnO Thin Films Prepared by Spray Pyrolysis on Glass Substrates at Various Temperatures for Integration in Solar Cell," *Energy Procedia,* vol. 74, pp. 529-538, 2015.

[41] D. Perednis and L. J. Gauckler, "Thin Film Deposition Using Spray Pyrolysis," *Journal of Electroceramics,* vol. 14, pp. 103-111, 2005.

[42] R. T. Ghahrizjani and M. H. Yousefi, "Effects of three seeding methods on optimization oftemperature, concentration and reaction time on opticalproperties during growth ZnO nanorods," *Superlattices and Microstructures,* vol. 112, pp. 10-19, 2017.

[43] M. Fang and Z. W. Liu, "Controllable size and photoluminescence of ZnO nanorod arrays on Sisubstrate prepared by microwave-assisted hydrothermal method," *Ceramics International,* vol. 43, pp. 6955-6926, 2017.

[44] M. Abdelfatah and A. El-Shaer, "One step to fabricate vertical submicron ZnO rod arrays by hydrothermalmethod without seed layer for optoelectronic devices," *Materials Letters,* vol. 210, pp. 366-369, 2018.

[45] X. Kong, Y. Hu and W. Pan, "Controllable preparation and photocatalytic activity of highly ordered ZnO," *Published in Micro & Nano Letters,* vol. 12, no. 7, pp. 461-465, 2017.

[46] J. H. Koo and B. W. Lee, "Hydrothermal synthesis of shaped ZnO nanostructures," *Journal of Ceramic Processing Research,* vol. 18, no. 2, pp. 156-160, 2017.

[47] S. Morkoc Karadeniz, B. Bozkurt Cirak, T. Kilinc, C. Cirak, M. Inal, Z. Turgut, A. E. Ekinci and M. Ertugrul, "A Comparative Study on Structural and Optical Properties of ZnO MicroNanorod Arrays Grown on Seed Layers Using Chemical Bath Deposition and SpinCoating Methods," *MATERIALS SCIENCE (MEDŽIAGOTYRA),* vol. 22, no. 4, pp. 476-480, 2016.

[48] E. A. Araujo Junior, F. X. Nobre, G. d. S. Sousa, L. S. Cavalcante, M. R. d. M. C. Santos, F. L. Souza and J. M. Elias de Matos, "Synthesis, growth mechanism, optical properties and catalytic activity of ZnO microcrystals obtained via hydrothermal processing," *RSC Advances,* vol. 7, pp. 24263-24281, 2017.

[49] L. R. Toporovska, A. M. Hryzak and B. I. Turko, "Photocatalytic properties of zinc oxide nanorods grown by different methods," *Optical and Quantum Electronics,* vol. 49, pp. 407-417, 2017.

[50] P. Li, B. Lu and Z. Luo, "Hydrothermal growth of wheatear-shaped ZnO microstructures and their photocatalytic activity," *Bulletin of Materials Science,* vol. 40, no. 6, pp. 1069-1074, 2017.

[51] X. Lv, Y. Du, Z. Li, Z. Chen, K. Yang, T. Liu, C. Zhu, M. Du and Y. Feng, "High photocatalytic property and crystal growth of spindle-like ZnO microparticles synthesized by one-step hydrothermal method," *Vacuum,* vol. 144, pp. 229-236, 2017.

[52] F. Bi, L. Zhao, L. Wang and G. Gai, "Multi-layer ZnO assembled microspheres, microstars and microflowers with high photocatalytic performance," *Journal of Materials Science: Materials in Electronics,* vol. 28, no. 11, pp. 7778-7783, 2017.

[53] V. N. Blaskov, I. D. Stambolova, K. I. Milenova, K. L. Zaharieva, L. D. Dimitrov, D. D. Stoyanova and A. E. Eliyas, "The photodegradation of Methylene Blue and Methyl Orange dyes and their mixture by ZnO obtained by hydrothermally activated precipitates," *Bulgarian Chemical Communication,* vol. 49, no. B, pp. 183-187, 2017.

[54] J. Gao, S. Huang, P. Luo and S. Huang, "Photocatalytic properties of ZnO micromaterials prepared by hydrothermal method," *Russian Journal of Physical Chemistry A,* vol. 90, no. 13, pp. 2665-2667, 2016.

[55] W. Q. Ma, Z. X. Gu, H. H. Nan, B. Y. Geng and X. J. Zang, "Morphology-controllable synthesis of 3D firecracker-like ZnO nanoarchitectures for high catalytic performance," *CrystEngComm,* vol. 17, no. 5, pp. 1121-1128, 2015.

[56] H. B. Lu, S. M. Wang, L. Zhao, J. C. Li, B. H. Dong and Z. X. Xu, "Hierarchical ZnO microarchitectures assembled by ultrathin nanosheets: hydrothermal synthesis and enhanced photocatalytic activity," *Journal of Materials Chemistry,* vol. 21, no. 12, pp. 4228-4234, 2011.

[57] R. F. Egerton, Physical Principles of Electron Microscopy, An Introduction to TEM, SEM, and AEM, vol. 2, Edmonton: Springer, 2016, pp. 1; 8-9; 15-16; 121-145.

[58] G. Dehm, J. M. Howe and J. Zweck, In-situ Electron Microscopy: Applications in Physics, Chemistry and Materials Science, vol. 1, Wiley-VCH, 2012, pp. 2-14.

[59] ARL Applied Research Laboratories S.A., Basics of X-ray Diffraction, Thermo ARL-CH, 1999.

[60] W. D. Callister, Materials Science and Engineering, 7 ed., New York: John Wiley & Sons, Inc., 2007, pp. 67-70.

[61] S. T. Thornton and A. Rex, Modern Physics for Scientists and Engineers, vol. 4, Cengage Learning, 2012.

[62] B. C. Smith, Quantitative Spectroscopy, Theory and Practice, Danvers: Academic Press, 2002, pp. 2-7.

[63] A. Primer, Fundamentals of UV-Visible Spectroscopy, Agilent Technologies, 2000, pp. 3-8; 11-13; 16-20; 30-33.

[64] J. Lu, H. Wang, D. Peng, T. Chen, S. Dong and Y. Chang, "Synthesis andpropertiesofAu/ZnO nanorodsasaplasmonic," *Physica E,* vol. 78, pp. 41-48, 2016.

[65] I. Oja, A. Mere, M. Krunks, R. Nisumaa, C. H. Solerbeck and M. Es-Souni, "Structural and electrical characterization pf TiO2 films by spray pyrolysis," *Thin Solid Films,* vol. 515, no. 2, pp. 674-677, 2006.

[66] R. E. Marotti, P. Giorgi, G. Machado and E. A. Dalchiele, "Crystallite size dependence of band gap energy for electrodeposited ZnO grown at different temperatures," *Solar Energy Materials and Solar Cells,* vol. 90, no. 15, pp. 2356-2361, 2006.